Computers and Fluids 167 (2018) 324–340

Contents lists available at ScienceDirect

Computers and Fluids

journal homepage: www.elsevier.com/locate/compfluid

Unsteady three-dimensional boundary element method for self-propelled bio-inspired locomotion

K.W. Moored

Department of Mechanical Engineering and Mechanics, Lehigh University, Bethlehem, PA 18015, USA

ARTICLE INFO

Article history:
Received 16 March 2017
Revised 12 January 2018
Accepted 13 March 2018
Available online 14 March 2018

Keywords:
Bio-inspired propulsion
Boundary element method
Panel method
Self-propelled swimming
Unsteady flows
Vortex dynamics

ABSTRACT

An unsteady three-dimensional boundary element method is developed to provide fast calculations of biological and bio-inspired self-propelled locomotion. The approach uniquely combines an unsteady three-dimensional boundary element method, a boundary layer solver and self-propelled equations of motion. This novel implementation allows for the self-propelled speed, power, efficiency and economy to be accurately calculated. A Dirichlet formulation is used with a combination of constant strength source and doublet elements to represent a deforming body with a nonlinearly deforming wake. The wake elements are desingularized to numerically stabilize the evolution of the wake vorticity. Weak coupling is used in solving the equations of motion and in the boundary layer solution. The boundary layer solver models both laminar and turbulent behavior along the deforming body to estimate the total skin friction drag acting on the body. The results from the method are validated with analytical solutions, computations and experiments. Finally, a bio-inspired self-propelled undulatory fin is modeled. The computed self-propelled speeds and wake structures agree well with previous experiments. The computations go beyond the experiments to gain further insight into the propulsive efficiency for self-propelled undulating fins. It is found that the undulating fin produces a time-averaged momentum jet at 76% of the span that accelerates fluid in the streamwise direction and in turn generates thrust. Additionally, it is discovered that high amplitude motions suppress the formation of a bifurcating momentum jet and instead form a single core jet. Consequently, this maximizes the amount of streamwise momentum compared to the amount of wasted lateral momentum and leads to a propulsive efficiency of 78% during self-propelled locomotion.

1. Introduction

Boundary element methods (BEMs) are a class of numerical methods used to solve boundary value problems throughout physics from electromagnetics [22] and fracture mechanics [36] to fluid flows at both low [37] and high Reynolds numbers [3]. In high Reynolds number flows they are classically described as panel methods and have been well established in the study of aerodynamics over several decades [20,24,29]. High Reynolds number BEMs assume that a fluid flow is incompressible, irrotational (except at singular elements) and inviscid, that is, a potential flow. This leads to simplified forms of the continuity and momentum equations that govern the fluid flow. Yet, unsteady BEM solutions are still rich with flow physics [39] and give accurate solutions at computational times that are several orders of magnitude faster than Navier–Stokes solvers [35,53].

Unsteady three-dimensional BEM computations have been used by many researchers to explore both biological and bio-inspired propulsion. The flight performance of birds [47] and the swimming performance of fin whales [27] and fish [9] have been examined to reveal features of high efficiency locomotion. For example, Zhu et al. [58] found that constructive or destructive interactions can occur between the shed vorticity from finlet structures and the caudal fin of tuna and giant danio. This can lead to enhanced thrust production or efficiency, respectively, with maximum efficiencies of 75% being calculated. More recently, Zhu [56] showed that spanwise and chordwise flexibility can enhance both thrust production and efficiency of a flapping wing. The benefit of flexibility was also found to be highly dependent upon the mass ratio between the wing and the surrounding fluid environment. Additionally, Zhu and Shoele [57], Shoele and Zhu [45,46] determined that the flexibility of ray-finned fish caudal and pectoral fins also improved their efficiency performance and reduced the time-varying lateral forces acting on the fish. Importantly, none of these previous studies have examined the locomotion of *self-propelled* swim-

E-mail addresses: kmoored@lehigh.edu, kwm213@lehigh.edu

https://doi.org/10.1016/j.compfluid.2018.03.045
0045-7930/

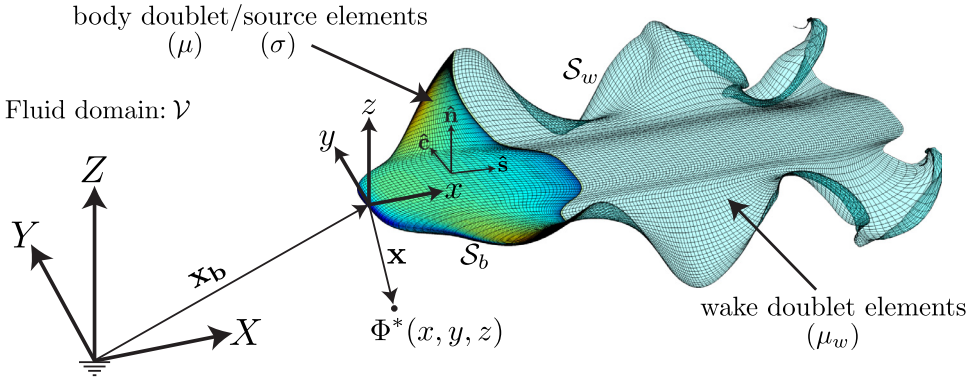

Fig. 1. The inertial reference frame fixed to the undisturbed fluid is denoted by (*X, Y, Z*) while the body-fixed reference frame is denoted by (*x, y, z*). The local normal, streamwise and cross-stream unit vectors are denoted by $\hat{\mathbf{n}}$, $\hat{\mathbf{s}}$, and $\hat{\mathbf{c}}$, respectively. The body surface, $\mathcal{S}_b$, is layered with distributions of doublet elements of strength μ and source elements of strength σ. The wake surface, $\mathcal{S}_w$, is layered with distributions of doublet elements of strength μ_w.

mers nor the *free-flight* of flyers, yet these conditions are a critical feature of bio-inspired locomotion.

One complicating factor is that an inviscid BEM does not inherently calculate viscous drag. This gives no opposing force to balance the thrust production, which leaves out a necessary ingredient for calculating a steady-state self-propelled speed. However, viscous drag has been estimated in several other BEM studies by using a boundary layer momentum-integral approach on streamwise strips [28,41,50]. Even with a viscous drag estimate included these studies focused on fixed freestream velocity conditions.

This work describes a novel implementation for computing the self-propelled performance of biological and bio-inspired propulsors within a BEM framework. There are three main components that must be combined to model self-propelled swimming: (1) a three-dimensional BEM fluid solver, (2) a boundary layer solver, and (3) an equations of motion solver. These components to the method are described in Section 2. Validation with several analytical, numerical and experimental solutions are presented in Section 3. Finally, comparison of the BEM solution with a three-dimensional self-propelled undulating fin experiment is presented in Section 4. The free-swimming performance and wake structures are shown to agree well with the experiments. Additionally, the self-propelled performance of cases that extend beyond the previous experiments are examined to provide novel physical insight into the self-propulsion of three-dimensional ray-inspired fins.

2. Computational methods

2.1. Governing equations and boundary conditions

To model a high Reynolds number fluid flow around a self-propelled bio-inspired device or animal an unsteady three-dimensional boundary element method is employed. The flow field is modeled as an incompressible, irrotational and inviscid flow, that is, a potential flow. For the self-propelled problem we define the problem in an inertial frame of reference that is attached to the undisturbed fluid (denoted by (*X, Y, Z*) in Fig. 1). As such the velocity field, $\mathbf{u}$, may be defined everywhere as the gradient of a scalar velocity potential,

$$\mathbf{u} = \nabla \Phi^*, \tag{1}$$

where Φ^* is defined in the inertial frame of reference and it is known as the perturbation potential. The pressure field, P, within this fluid can be calculated from the unsteady Bernoulli equation,

$$P(X,Y,Z,t) = -\rho \frac{\partial \Phi^*}{\partial t}\bigg|_{inertial} - \rho \frac{\left(\nabla \Phi^*\right)^2}{2}, \tag{2}$$

which is formulated in the inertial frame where the reference pressure $P_\infty = 0$ and the perturbation potential at infinity is zero. Also, ρ is the fluid density. The time derivative of the perturbation potential for a point on the surface of the body is then calculated by using a body-fixed Lagrangian frame (denoted by (x,y,z) in Fig. 1) [9,35,54], that is,

$$P(x,y,z,t) = -\rho \frac{\partial \Phi^*}{\partial t}\bigg|_{body} + \rho(\mathbf{u_{rel}} + \mathbf{U_0}) \cdot \nabla \Phi^* - \rho \frac{\left(\nabla \Phi^*\right)^2}{2}. \tag{3}$$

The translational velocity of a body-fixed frame of reference is $\mathbf{U_0}$ while the relative velocity of a point on the surface of the body to the body-fixed reference frame is $\mathbf{u_{rel}}$. Once the perturbation potential is known, then the pressure on the body surface may be found and the forces can be calculated by integrating the pressure and shear stress, τ, acting on the body.

$$\mathbf{F}(x,y,z,t) = \int_{\mathcal{S}_b} \left(-P\,\hat{\mathbf{n}} + \tau\,\hat{\mathbf{s}}\right) d\mathcal{S} \tag{4}$$

The body surface is denoted as $\mathcal{S}_b$, the outward normal vector from the body surface is $\hat{\mathbf{n}}$ and the tangential vector along the body surface in the streamwise direction is $\hat{\mathbf{s}}$. This inviscid formulation is coupled to a viscous boundary layer solver described in Section 2.9, which estimates the shear stress acting on the body in the streamwise direction produced by the outer potential flow. Note that the shear stress acting in the cross-stream direction is not accounted for in the viscous boundary layer solver and is therefore not present in Eq. (4). The problem is then reduced to solving for the perturbation potential throughout the fluid, which is governed by Laplace's equation,

$$\nabla^2 \Phi^* = 0. \tag{5}$$

The boundary conditions that must be satisfied for an inviscid fluid are that there is no fluid flux through the body surface and that the flow disturbances caused by the body must decay far away,

$$\mathbf{n} \cdot \nabla \Phi^* = \mathbf{n} \cdot (\mathbf{u_{rel}} + \mathbf{U_0}) \qquad \text{on } \mathcal{S}_b \tag{6}$$

$$\nabla \Phi^*\Big|_{|\mathbf{x}|\to\infty} = 0 \qquad \text{on } \mathcal{S}_\infty \tag{7}$$

where $\mathcal{S}_\infty$ is the surface at infinity bounding the fluid and $\mathbf{x} = [x, y, z]^T$ is measured from the body-fixed frame of reference.

2.2. Boundary integral equation

A general solution to Laplace's equation for the potential anywhere within the fluid domain, $\mathcal{V}$, can be determined. This is done

by considering the potential response at a point $\mathbf{x} = [x, y, z]^T$ due to a source located at $\mathbf{x_0} = [x_0, y_0, z_0]^T$, that is, the infinite space Green's function which satisfies the Poisson equation with homogeneous far-field boundary conditions [19]. The infinite space Green's function in three dimensions is then,

$$G(\mathbf{x}; \mathbf{x_0}) = -\frac{1}{4\pi r}, \qquad \text{where } r = |\mathbf{x} - \mathbf{x_0}|, \tag{8}$$

where r is the distance between the point of interest and the source point. By invoking Green's formula twice with respect to the perturbation potential within the fluid volume, Φ^*, the internal perturbation potential within the volume enclosed by $\mathcal{S}_b$, Φ_i^*, and the Green's function and then adding the results, the following boundary integral equations (BIEs) for the internal or external perturbation potential are derived,

$$\Phi_i^*(\mathbf{x}) = \iint_{\mathcal{S}_b} \left[\sigma(\mathbf{x_0})\, G(\mathbf{x}; \mathbf{x_0}) - \mu(\mathbf{x_0})\, \hat{\mathbf{n}} \cdot \nabla G(\mathbf{x}; \mathbf{x_0})\right] d\mathcal{S}_0 - \iint_{\mathcal{S}_w} \mu_w(\mathbf{x_0})\, \hat{\mathbf{n}} \cdot \nabla G(\mathbf{x}; \mathbf{x_0})\, d\mathcal{S}_0 \tag{9}$$

$$\Phi^*(\mathbf{x}) = \iint_{\mathcal{S}_b} \left[\sigma(\mathbf{x_0})\, G(\mathbf{x}; \mathbf{x_0}) - \mu(\mathbf{x_0})\, \hat{\mathbf{n}} \cdot \nabla G(\mathbf{x}; \mathbf{x_0})\right] d\mathcal{S}_0 - \iint_{\mathcal{S}_w} \mu_w(\mathbf{x_0})\, \hat{\mathbf{n}} \cdot \nabla G(\mathbf{x}; \mathbf{x_0})\, d\mathcal{S}_0 \tag{10}$$

where,

$$\sigma(\mathbf{x_0}) = \hat{\mathbf{n}} \cdot \nabla\left(\Phi^* - \Phi_i^*\right) \tag{11}$$

$$-\mu(\mathbf{x_0}) = \Phi^* - \Phi_i^* \tag{12}$$

$$-\mu_w(\mathbf{x_0}) = \Phi_+^* - \Phi_-^* \tag{13}$$

The surface boundary integral is broken up into an integral over the body boundary, $\mathcal{S}_b$, the wake boundary, $\mathcal{S}_w$, and the far-field boundary, $\mathcal{S}_\infty$. To formulate the problem in an inertial frame of reference attached to the undisturbed fluid the contribution to the potential from the farfield boundary is set to zero, that is $\Phi_\infty = 0$. The potential jump $\mu(\mathbf{x_0})$ represents the strength of a dipole or doublet while the jump in the normal derivative of the potential $\sigma(\mathbf{x_0})$ represents the strength of a source. The wake boundary in the limit as it becomes infinitesimally thin has a continuous normal derivative of the potential so it does not support a source distribution. The local potential jump between the top and bottom surface of the wake is represented by $\mu_w(\mathbf{x_0})$, where Φ_+^* is the potential above the wake and Φ_-^* is the potential below the wake. During the derivation of the boundary integral equation the source and observation locations switch roles. Note that when this happens $G(\mathbf{x_0}; \mathbf{x}) = G(\mathbf{x}; \mathbf{x_0})$ due to the reciprocity of the Green's function, however, $\nabla G(\mathbf{x_0}; \mathbf{x}) = -\nabla G(\mathbf{x}; \mathbf{x_0})$.

The general solution to the potential flow problem in a fluid domain $\mathcal{V}$ is now reduced to finding a distribution of sources and doublets on the boundaries $\mathcal{S}_b$ and $\mathcal{S}_w$ that satisfy the boundary conditions. Since the continuity and thus Laplace's equation is time-independent, all of the time-dependency comes from the unsteady Bernoulli equation and the time-dependent boundary conditions.

2.3. Enforcement of the boundary conditions

The elementary solutions of the doublet and source both implicitly satisfy the far-field boundary condition. In this paper, the no-flux condition on the body is satisfied with an indirect Dirichlet formulation since it saves computational effort as compared to the Neumann formulation [24]. For the Dirichlet problem, we set the internal potential to a constant, which in our case is selected to be zero

$$\Phi_i^* = 0. \tag{14}$$

To enforce this condition the BIE must be satisfied with the left-hand side equal to zero. This condition also leads to the simplification of the source and doublet strength equations, which become

$$-\mu = \Phi^* \tag{15}$$

$$\sigma = \nabla\Phi^* \cdot \mathbf{n} = (\mathbf{u_{rel}} + \mathbf{U_0}) \cdot \mathbf{n}. \tag{16}$$

The perturbation velocity on the surface of the body is simplified and can be found by a local differentiation of the perturbation velocity potential,

$$\mathbf{u_b} = \nabla\Phi_b^* = \frac{\partial\Phi*}{\partial s}\,\hat{\mathbf{s}} + \frac{\partial\Phi*}{\partial c}\,\hat{\mathbf{c}} + \frac{\partial\Phi*}{\partial n}\,\hat{\mathbf{n}} = -\frac{\partial\mu}{\partial s}\,\hat{\mathbf{s}} - \frac{\partial\mu}{\partial c}\,\hat{\mathbf{c}} + \sigma\,\hat{\mathbf{n}}, \tag{17}$$

where $\hat{\mathbf{c}}$ is the tangential vector along the surface in the cross-stream direction. The pressure over the body can also be found in terms of the boundary element strengths,

$$P_b(x, z, t) = \rho\frac{\partial\mu}{\partial t}\bigg|_{body} + \rho(\mathbf{u_{rel}} + \mathbf{U_0}) \cdot \mathbf{u_b} - \rho\frac{\mathbf{u_b}^2}{2}. \tag{18}$$

Now, the problem is reduced to finding a distribution of sources and doublets that solve the BIE when the Dirichlet condition is applied.

2.4. Numerical solution

To numerically solve this problem, the boundaries are discretized into constant strength quadrilateral boundary elements distributed over the body and wake. Then the boundary integral Eq. (9) with the Dirichlet condition substituted (Eq. (14)) can be discretized into the summation over the boundary elements,

$$\sum_{j=1}^{N_b} B_{ij}\sigma_j + \sum_{j=1}^{N_b} C_{ij}\mu_j + \sum_{k=1}^{N_w} C_{w,ik}\mu_{w,k} = 0 \tag{19}$$

with,

$$B_{ij} = -\frac{1}{4\pi}\int_{ele}\frac{1}{|\mathbf{r_{ij}}|}\,\mathrm{d}\mathcal{S}_0 \tag{20}$$

$$C_{ij} = -\frac{1}{4\pi}\int_{ele}\frac{\hat{\mathbf{n}} \cdot \mathbf{r_{ij}}}{|\mathbf{r_{ij}}|^3}\,\mathrm{d}\mathcal{S}_0 \tag{21}$$

$$C_{w,ik} = -\frac{1}{4\pi}\int_{ele}\frac{\hat{\mathbf{n}} \cdot \mathbf{r_{ik}}}{|\mathbf{r_{ik}}|^3}\,\mathrm{d}\mathcal{S}_0 \tag{22}$$

$$\text{and} \quad \mathbf{r_{ij}} = \mathbf{x_i} - \mathbf{x_{0,j}}, \quad \mathbf{r_{ik}} = \mathbf{x_i} - \mathbf{x_{0,k}} \tag{23}$$

where N_b is the number of body elements, N_w is the number of wake elements, $\int_{ele}$ represents the integration over a single boundary element, $d\mathcal{S}_0$ is the differential area of a boundary element, $\mathbf{x_i}$ is the vector denoting the position of the ith collocation point, $\mathbf{x_{0,j}}$ is the vector denoting the position of a differential area of the jth element and $\mathbf{x_{0,k}}$ is the vector denoting the position of a differential area of the kth element. Explicit solutions for the influence integrals over the elements can be found in Katz and Plotkin [24]. Eq. (19) must be satisfied at every point within the boundary $\mathcal{S}_b$, which in the discretized form are satisfied at N_b collocation points. In the current method, the collocation points were located at the

center of the elements but moved into the body by 15% of the distance of the half-thickness of the body at that point, along the element normal vector. The system of equations (19), however, needs to be modified by an explicit or implicit Kutta condition to allow the support of bound circulation. Also, for time-stepping, a wake shedding procedure must be used to satisfy Kelvin's condition.

2.5. Wake model

In this work an explicit Kutta condition is chosen for its simplicity. A trailing-edge element is the first element in the set of wake doublet elements that connects the wake surface to the body surface at the trailing edge and it is used to enforce the Kutta condition of finite velocity there. This occurs by setting the strength of the trailing-edge element such that it cancels the vorticity at the trailing-edge. The strength of the trailing-edge element is then found at each time step from the difference in strengths between the top and bottom body doublet elements that intersect the trailing edge, i.e.,

$$\mu_{w,TE} = \mu_{t,TE} - \mu_{b,TE}. \tag{24}$$

The orientation of the trailing-edge element is set to be along a line that bisects the angle of the trailing-edge, which is typical for steady flow conditions [24]. Traditionally, the trailing-edge element length is set to 0.3 – $0.5\,U_0\Delta t$ [54], where Δt is the time step. Here a length of $0.4\,U_0\Delta t$ was used since it gave good solution convergence while maintaining solution accuracy with the validation cases. During each time step the trailing-edge element from the previous time step is 'shed' a distance $U_0\Delta t$ downstream and it becomes the second wake element. The strength of that wake element is the same as the strength of the previous trailing-edge element and it remains constant for all subsequent time steps. The trailing-edge element's strength can be re-written in terms of the unknown body element strengths using Eq. (24) and the discretized BIE is then modified, that is,

$$\sum_{j=1}^{N_b} A_{ij}\mu_j = -\sum_{j=1}^{N_b} B_{ij}\sigma_j - \sum_{k=2}^{N_w} C_{w,ik}\mu_{w,k} \tag{25}$$

with,

$$A_{ij} = \begin{cases} C_{ij} - C_{w,i1}, & \text{j = bottom element} \\ C_{ij} + C_{w,i1}, & \text{j = top element} \\ C_{ij}, & \text{otherwise} \end{cases}$$

Now, the body source element strengths and wake element strengths are known. The linear set of equations may be solved at each time step for the body doublet strengths, μ_j, by an inversion of matrix A_{ij}. The trailing-edge element strengths are then directly calculated from the body doublet element strengths. In the current method, the number of unknown body doublet element strengths is reduced in half by assuming left-right symmetry for the problem and using mirror image elements to represent the left-half of the body and the wake.

2.6. Nonlinear wake deformation

The wake elements that are shed at each time step model the shedding of vorticity from the body into its wake. These elements cannot support loads so they must be free to advect with the local velocity field. At each time step the induced velocity at the corner points of each wake element, $\mathbf{u}_w$, is determined. The wake element corner points are then displaced by $\Delta\mathbf{d} = \mathbf{u}_w\Delta t$. Calculating the induced velocity at the wake element corner points will lead to a numerically unstable solution if the doublet elements are not desingularized. Here we take advantage of the equivalence of a constant strength doublet element and a vortex ring around the edge of that element by using the desingularized Biot-Savart law,

$$\mathbf{u}(\mathbf{x}) = \frac{\Gamma}{4\pi}\oint \frac{\mathbf{s}\times\mathbf{r}}{r^3+\delta^3}\,ds, \tag{26}$$

to calculate the induced velocity field [25]. Here, the circulation of an element is $\Gamma = -\mu$ and the desingularization parameter, δ, is a constant and a free-parameter for the method. Provided that δ is large enough, the transfer of energy to high wavenumbers is minimized thereby preventing solution breakdown [58]. The desingularization parameter mimics the effect of viscosity in a real fluid by giving each vortex ring element a core radius directly related to δ.

2.7. Lumped wake elements

A lumped wake element model is used to restrict the growth of the problem size as the number of wake elements increases with every time step. The lumped elements conserve the net circulation in the wake such that Kelvin's condition still holds. There is one lumped wake element for every trailing-edge element, with the trailing-edge elements acting as the wake element generators and the lumped elements acting as wake element absorbers in the far-field. The strength of the lumped elements at the nth time step is the summation of the circulation of the lump elements at the previous time step and the absorbed elements at the nth time step.

$$\Gamma^n_{lump} = \Gamma^{n-1}_{lump} + \Gamma^n_{w,absorbed} \tag{27}$$

The lumped element corner point locations, $\mathbf{p}_{lump}$, are at the weighted-average locations of the absorbed elements where the weights are based on the magnitude of the increment of circulation added to the lumped element compared to the total absorbed magnitude of circulation,

$$\mathbf{p}^n_{lump} = \left[\frac{\Gamma^{n-1}_{mag}}{\Gamma^n_{mag}}\right]\mathbf{p}^{n-1}_{lump} + \left[\frac{|\Gamma^n_{w,absorbed}|}{\Gamma^n_{mag}}\right]\mathbf{p}^n_{absorbed} \tag{28}$$

with,

$$\Gamma^n_{mag} = \Gamma^{n-1}_{mag} + |\Gamma^n_{w,absorbed}|$$

The lumped elements absorb wake elements such that the most recent N_l oscillation cycles of wake elements remain to fully-resolve the near wake. It is found that by measuring the time-averaged forces on the body, the lumped wake solution is within 1% of the fully-resolved solution if $N_l \geq 4$ for two-dimensional flows and $N_l \geq 2$ for three-dimensional flows. The lumped wake elements are included in the third term of Eq. (25).

2.8. Equations of motion

To be able to calculate the self-propelled body dynamics and performance of a bio-inspired device or an animal, the equations of motion for the body must be solved. For the results in this work, we only allow streamwise translation to be unconstrained while the other degrees of freedom undergo fully prescribed motions. To further simplify the implementation of the unconstrained body dynamics, a loose or one-way coupling with the fluid solution is used. That is, the forces from the solution of the BEM fluid problem are used as the driving forces in the equations of motion. The body frame velocity and position is then explicitly determined without sub-iterations between the fluid solver and the body dynamics solver. Following [5], the loose-coupling scheme uses the x-position of the body frame (Fig. 1) and the body frame velocity at the current time step, x^n_b and U^n_0, respectively, to explicitly solve for the position, x^{n+1}_b, and velocity, U^{n+1}_0, at the subsequent time step,

$$x^{n+1}_b = x^n_b + \frac{1}{2}\left(U^{n+1}_0 + U^n_0\right)\Delta t, \tag{29}$$

$$U_0^{n+1} = U_0^n + \frac{F_x^n}{M}\Delta t. \tag{30}$$

Here the streamwise force acting on the body at the current time step is F_x^n and the mass of the body is M.

2.9. Viscous boundary layer solver

An estimate of skin friction drag is critical to computing self-propelled body dynamics and performance as this is the main source of drag for streamlined swimmers. Using the potential outer flow solution, the boundary layer properties and the skin friction can be estimated without an assumption on the form of a drag law acting on a body. To calculate the boundary layer properties a two-dimensional von Kármán momentum integral analysis is performed over streamwise strips along the body. Some three-dimensionality is embedded into the analysis by using an effective outer flow velocity at each chordwise station, q_o, which is the magnitude of the streamwise and cross-stream tangential velocities at those locations,

$$|q_o| = \sqrt{q_s^2 + q_c^2} \tag{31}$$

This analysis can be used to approximate the boundary layer displacement thickness and the skin friction drag coefficient over each boundary element based on the local outer flow alone. The outer flow is coupled to the boundary layer solution in a loose coupling, that is, there are no sub-iterations between the outer flow solution and the shape of the body based on the displacement thickness of the boundary layer. From the outer flow solution the stagnation point on the body is determined for each strip. Then based on the stagnation point the surface is divided into an upper and lower part where each boundary layer begins growing. First, the method of Thwaites [41] is used to solve for the laminar boundary layer properties where the momentum thickness, θ, can be determined by,

$$\theta^2 = 0.45\frac{\nu}{q_o^6}\int_{x_{stag}}^{x} q_o^5\, dx. \tag{32}$$

Here, ν is the kinematic viscosity, x_{stag} is the location of the stagnation point, x is a position along the upper or lower surface. Additionally, Thwaites defined the non-dimensional pressure gradient parameter as,

$$\lambda \equiv \frac{\theta^2}{\nu}\frac{dq_o}{dx}. \tag{33}$$

This is used to determine where laminar separation occurs, which happens when $\lambda < -0.09$. When λ is limited to only have a minimum value of -0.09, then this limited dimensionless pressure gradient parameter can be used to calculate the shear function, S, and the skin friction drag coefficient, C_f, that is,

$$S = (\lambda + 0.09)^{0.62} \tag{34}$$

$$C_f = \frac{2\nu S}{q_o\theta} \tag{35}$$

where: (36)

$$C_f \equiv \frac{\tau}{1/2\,\rho q_o^2} \tag{37}$$

Here τ is the shear stress acting on the body.

Next Cebeci and Smith's criterion [52] is used to determine the location of transition to a turbulent boundary layer. This method calculates the transition location from an empirical relation based on the Reynolds numbers, $Re_\theta = q_o\theta/\nu$, and $Re_x = q_o x/\nu$. Transition occurs along an airfoil when,

$$Re_\theta > 1.174\left(1 + \frac{22,400}{Re_x}\right)Re_x^{0.46}. \tag{38}$$

Transition typically occurs over a short distance of an airfoil, so we approximate the transition distance to be zero following [41].

Finally, to calculate the skin friction drag from the turbulent boundary layer with pressure gradients, the Kármán momentum integral relation,

$$\frac{d\theta}{dx} + (2+H)\frac{\theta}{q_o}\frac{dq_o}{dx} = \frac{C_f}{2}, \tag{39}$$

along with a skin friction empirical correlation,

$$C_f \approx \frac{0.3e^{-1.33H}}{(\log_{10} Re_\theta)^{1.74+0.31H}}, \tag{40}$$

are used [52], where H is the shape factor. In order to close these relations a third equation must be introduced then the ordinary differential Eq. (39) is solved for the momentum thickness. In the current boundary layer solver formulation the shape factor is approximated as $H \approx 1.28$, which comes from a one-seventh-power law velocity profile assumption that is accurate for flat plate turbulent boundary layers with no pressure gradient [24]. It is noted that this simple approximation can be improved with more accurate closure such as one based on entrainment relations [8].

2.10. Method limitations

The BEM is a fast numerical method that is useful for calculations that involve approximately inviscid flow physics such as high Reynolds number flows over streamlined bodies. Viscosity can introduce two major complications for the BEM: (1) the generation of skin friction drag and (2) the separation of shear layers over a body. The former is addressed in the current study by using a momentum integral analysis to calculate skin friction. However, it should be noted that this analysis assumes quasi-two-dimensional boundary layers, which may not be a good approximation for all flows. Even if there are two-dimensional boundary layers the boundary layer solution is highly sensitive to the model used to calculate the location of transition to a turbulent boundary layer. The latter complication of separation over a body is difficult to simulate with a BEM, although recent work with two-dimensional BEMs show great promise in this regard [35,40]. Modeling separation in three-dimensional flows is more difficult, but there has been some moderate success in the past [41]. Additionally, conventional BEM implementations solve dense matrices with computational times that scale with the number of elements, N, as $\mathcal{O}(N^2)$. This can limit the number of elements that are used to resolve a flow, but the scaling of computational time can be reduced to $\mathcal{O}(N)$ or $\mathcal{O}(N\log(N))$ with GPU or Fast-Multipole acceleration [54].

3. Numerical method validation

To validate the current boundary element method implementation a series of analytical, numerical and experimental results are used to analyze the accuracy of the current numerical method. The validation cases include a two-dimensional steady and unsteady flow case, a two-dimensional unsteady waving plate case, a three-dimensional steady and unsteady flow case, a skin friction drag case, a self-propelled biological propulsion case and a self-propelled bio-inspired undulating fin case.

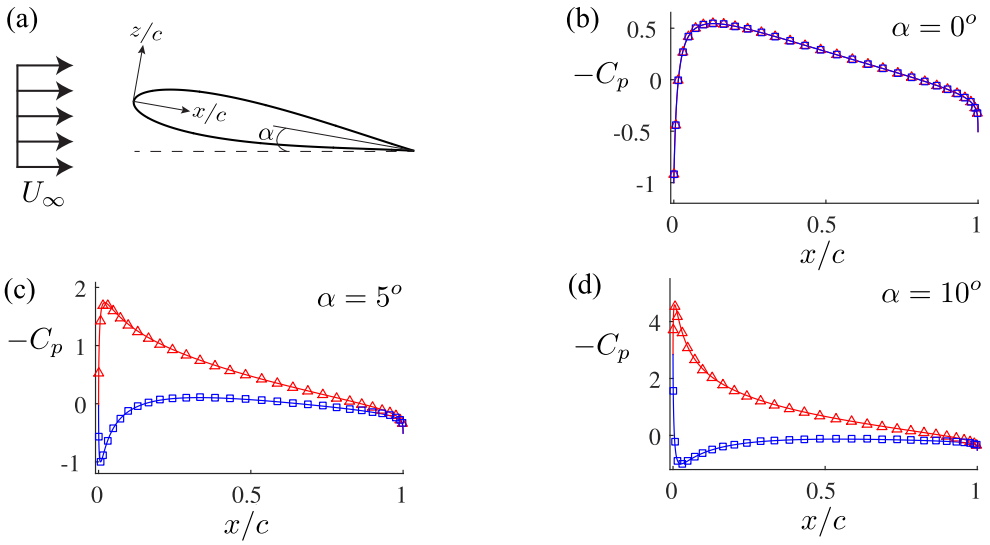

Fig. 2. (a) Schematic of a 15% thick van de Vooren airfoil at an angle of attack, α, in a steady flow, U_∞. The coefficient of pressure over the top and bottom surface of the airfoil for three angles of attack: (b) $\alpha = 0^0$, (c) $\alpha = 5^0$ and (d) $\alpha = 10^0$. The analytical solution for the top surface is represented by the solid red line while the numerical solution is represented by the red triangles. For the bottom surface, the analytical solution is represented by the solid blue line and the numerical solution is represented by the blue squares. (For interpretation of the references to color in this figure legend, the reader is referred to the web version of this article.)

3.1. Two-dimensional steady flow

The steady pressure distribution over a two dimensional van de Vooren airfoil is first examined. The van de Vooren airfoil shape is chosen since there is an exact analytical solution for its pressure distribution [49] and since it has a finite-angle trailing edge as opposed to the cusped trailing edge of a Joukowski airfoil. Cusped trailing edges are numerically difficult to obtain accurate solutions when using a Dirichlet formulation. A detailed description of the solution for the pressure distribution around a van de Vooren shaped airfoil can be found in Katz and Plotkin [24]. The analytical solution uses the van de Vooren conformal mapping to represent a finite thickness airfoil at an angle of attack in a potential flow (Fig. 2(a)). The flow around the airfoil is assumed to be inviscid, irrotational and incompressible. Additionally, the starting vortex is assumed to be infinitely far away making the flow steady as well.

The current unsteady three-dimensional formulation is used to solve this two-dimensional steady flow problem by solving for the flow over a van de Vooren wing with a rectangular planform shape and an aspect ratio of 1000. The wing is discretized into 30 chordwise boundary elements for both the top and bottom surfaces and 50 spanwise boundary elements for a total of 3000 body elements. The computation is discretized into 10 timesteps with the elapsed time for each step being $\Delta t = 100$ s. The starting vortex present in the unsteady numerical solution is 1000 chord lengths downstream of the wing since the total elapsed time for the simulations is $\Delta t_{total} = 1000$ s, the free-stream velocity is $U_\infty = 1$ m/s and the chord length of the wing is $c = 1$ m. This is necessary since the analytical solution assumes that the starting vortex is infinitely far away.

The coefficient of pressure over the wing is calculated for the section nearest the symmetry plane or mid span of the wing where the flow is nearly two-dimensional. Fig. 2(a) shows a schematic of the physical problem where a 15% thick van de Vooren wing is placed in a steady flow of U_∞ and an angle of attack, α. Fig. 2(b)–(d) compares the exact solutions (solid lines) to the numerical BEM solutions (square and triangle markers). For $\alpha = 0^\circ$, the pressure coefficient is observed to stagnate at the leading edge ($C_p = 1$). Subsequently, the pressure drops as flow is accelerated symmetrically over the top and bottom surfaces until a minimum pressure of $C_p = -0.5$ is reached around $x/c = 0.2$ near the maximum thickness. After the maximum thickness location there is a gradual pressure recovery of the flow to the trailing edge. For $\alpha > 0^\circ$, a prominent leading-edge suction peak can be observed that grows with increasing α. Importantly, there is excellent agreement between the analytical and numerical solutions over a range of angles of attack from $\alpha = 0$ – 10°.

3.2. Two-dimensional unsteady flow

The unsteady lift produced by a two-dimensional thin airfoil heaving with small amplitude motion is examined next. Theodorsen [48] provided an analytical solution to this problem and a schematic detailing the problem is shown in Fig. 3(a). Theodorsen's theory assumes that a thin airfoil is harmonically oscillating in a potential flow where the flow is inviscid, irrotational, and incompressible. The theory also assumes small amplitudes of motion and that the wake is non-deforming and planar, that is, it lies along the x-axis. Under these assumptions a theoretical model for the lift of a harmonically heaving airfoil can be derived and cast into a non-dimensional form,

$$c_l = -2\pi^2\, St\, |C(k)|\, \cos(2\pi t/T + \phi) + \pi^2 St\, k\, \sin(2\pi t/T) \quad (41)$$

where,

$$c_l = \frac{L}{1/2\ \rho c U_\infty^2} \quad h = h_0\, \sin(2\pi t/T) \quad St = \frac{2h_0 f}{U_\infty} \quad k = \frac{\pi f c}{U_\infty}$$

Here, h is the time varying heave, h_0 is the heave amplitude, L is the instantaneous lift, f is the frequency of motion, T is the period of motion, $|C(k)|$ is the magnitude and ϕ is the phase angle of the lift deficiency factor, which is a complex number. Also, St and k are the Strouhal number and reduced frequency, respectively. A 0.1% thick symmetric NACA airfoil was used to simulate an infinitesimally thin plate. The parameters used were $c = 1$ m, $U_\infty = 1$ m/s, $h_0/c = 0.001$ with two cases of $St = 0.001$, $k = \pi/2$ and $St = 0.01$, $k = 5\pi$. The three-dimensional formulation is used to solve this two-dimensional unsteady problem by solving for the flow over a NACA wing with a rectangular planform shape and an aspect ratio of 1000. The lift coefficient from the numerical solution is then normalized by the planform area instead of the chord length as in

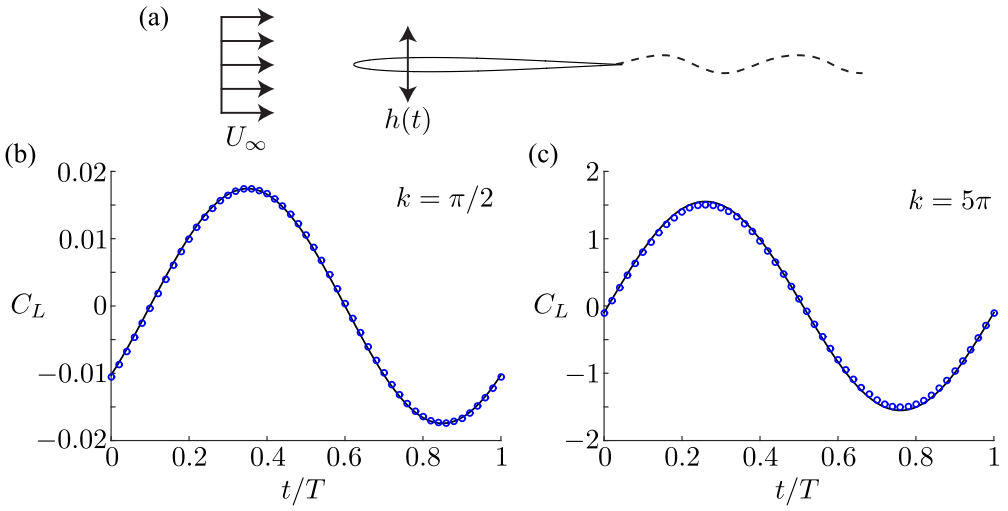

Fig. 3. Comparison of the numerical solution marked by circles (o) with the Theodorsen model denoted by the solid line (–). The parameters of $c = 1$, $U_\infty = 1$ m/s, $h/c = 0.001$ were used for both graphs while the left graph used $St = 0.001$ and $k = \pi/2$ and the right graph used $St = 0.01$ and $k = 5\pi$. The period of motion is $T = 1/f$.

the Theodorsen model. The wing was discretized into 50 chordwise boundary elements for both the top and bottom surfaces and 40 spanwise boundary elements for a total of 4000 body elements. The computation was discretized into 50 time steps per oscillation cycle for 4 cycles. This gives a time step size of $\Delta t = 0.04$ s and $\Delta t = 0.004$ s for the $k = \pi/2$ and $k = 5\pi$ cases, respectively. The force calculations were taken from the fourth oscillation cycle. A non-deforming wake was used to simulate the assumptions in the Theodorsen model. Fig. 3 shows excellent agreement between the time-varying lift coefficients of the analytical and numerical solutions. The BEM solution of the time-varying lift coefficient for a Strouhal number of $St = 0.01$ has a slightly lower peak lift coefficient of $C_L = 1.505$ compared to the Theodorsen model of $c_l = 1.545$, which is also seen in other studies [54].

3.3. Two-dimensional unsteady waving plate flow

Later in Section 4, results from a three-dimensional undulating fin will be presented. In order to validate the accuracy of the current BEM formulation to properly simulate the deforming traveling-wave kinematics of an undulating fin, the numerical formulation has been compared to Wu's theory [55]. This theory analytically solves for the time-averaged thrust, power and efficiency of a two-dimensional waving plate with an arbitrary amplitude envelope. The theory has the typical potential flow assumptions, that is, an incompressible, irrotational and inviscid flow. It also assumes that the amplitude of the motion is small, the plate is infinitesimally thin and the wake that is shed is non-deforming and planar. Under these assumptions and the special case of a constant amplitude envelope (Fig. 4(a)), Wu's theory reduces to the following,

$$c_t = \pi A_0^2(\Omega\Omega_* + QQ_*), \tag{42}$$

$$c_p = \pi A_0^2\left(\Omega\Omega_* + QQ_* + \left\{F(k) - \left[F(k)^2 + G(k)^2\right]\right\}\left\{N_0^2 + N_1^2\right\}\right), \tag{43}$$

$$\eta = c_t/c_p, \qquad c_t = \frac{\overline{T}}{1/2\,\rho U^2 c}, \qquad c_p = \frac{\overline{P}}{1/2\,\rho U^3 c}, \tag{44}$$

where:

$$\Omega = (k-k_x)[F(k)J_0(k_x) + G(k)J_1(k_x)], \quad \Omega_* = \Omega + k_x J_0(k_x),$$
$$Q = (k-k_x)\{[1-F(k)]J_1(k_x) + G(k)J_0(k_x)\}, \quad Q_* = Q + k_x J_1(k_x),$$
$$N_0 = (k-k_x)J_0(k_x), \quad N_1 = (k-k_x)J_1(k_x),$$

and:

$$z(x,t) = \frac{cA_0}{2}\cos(\omega t - 2k_x x/c), \quad \omega = 2\pi f, \quad k_x = \frac{\pi c}{\lambda}, \quad k = \frac{\pi f c}{U}.$$

Here k is the reduced frequency, k_x is the wavenumber, A_0 is the non-dimensional wave amplitude, λ is the wavelength, c is the chord length, f is the oscillation frequency, ρ is the fluid density, U is the freestream velocity, $F(k)$ and $G(k)$ are the real and imaginary parts of Theodorsen's lift deficiency function, respectively, and $J_0(k_x)$ and $J_1(k_x)$ are Bessel functions of the first kind.

In order to closely follow the assumptions of the theory a NACA airfoil with a maximum thickness-to-chord ratio of $b/c = 0.02$ was used to simulate a flat plate. A 2% thickness was chosen to be as thin as possible, but sufficiently thick so that there is a well-defined leading-edge in order to avoid numerical sensitivity in the thrust calculation. The parameters used were $c = 1$ m, $U = 1$ m/s, $A_0 = 0.03$ and 0.05, $k = 1$, 2, and 3, and $k_x = 0$, 0.25, and 0.5. The reduced frequency and wavenumber ranges were chosen to closely match the ranges used for the undulating fin described in Section 4. The three-dimensional formulation is used to solve this two-dimensional unsteady problem by solving for the flow over a NACA wing with a rectangular planform shape and an aspect ratio of 1000. The thrust and power coefficients from the numerical solution is then normalized by the planform area instead of the chord length as in the Wu model. The wing was discretized into 125 chordwise boundary elements for both the top and bottom surfaces and 40 spanwise boundary elements for a total of 10000 body elements. The computation was discretized into 60 time steps per oscillation cycle for 4 cycles. This gives a time step size of $\Delta t = 0.052$, 0.026, and 0.017 s for the $k = 1$, 2, and 3 cases, respectively. The force calculations were taken from the fourth oscillation cycle. A non-deforming wake was used to simulate the assumptions in Wu's theory.

Fig. 4(b)–(d) presents the propulsive efficiency, thrust coefficient, and power coefficient from the BEM simulations (markers) compared with Wu's theory (solid lines). The triangle and square markers represent the non-dimensional amplitudes of $A_0 = 0.03$ and 0.05, respectively. Additionally, the wavenumbers $k_x = 0$, 0.25, and 0.5 are represented with a gradient of colors from black to white where black is $k_x = 0$ and white is $k_x = 0.5$. There is excellent agreement between the efficiency, thrust, and power of the analytical and numerical solutions. The BEM solution slightly over and under predicts the power and efficiency, respectively, of

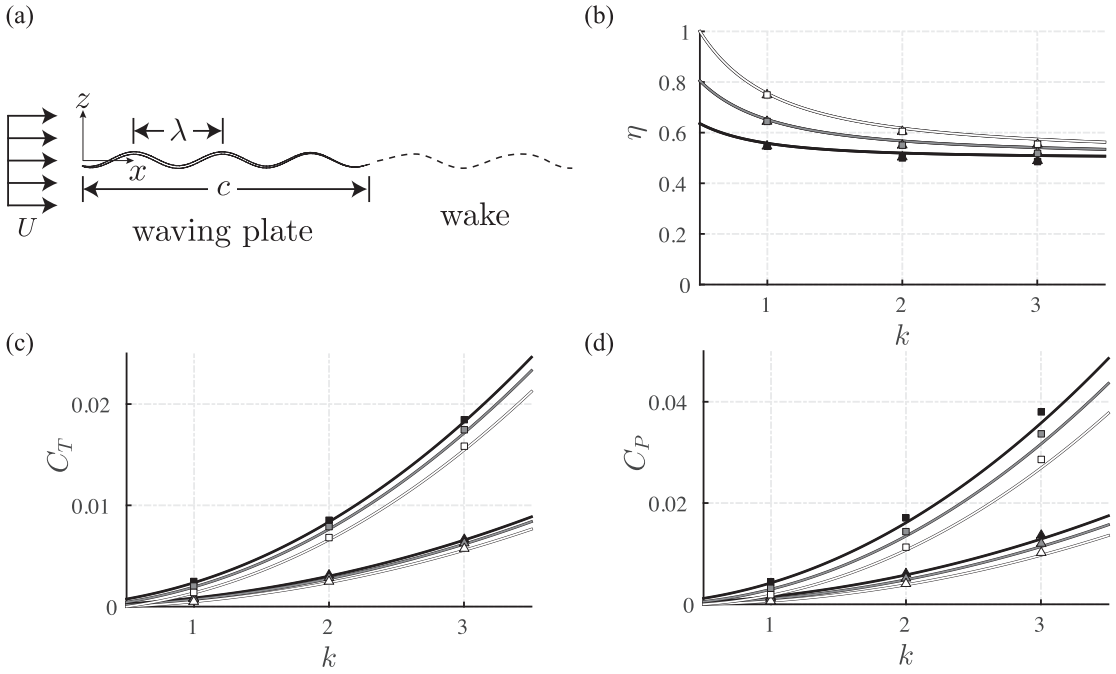

Fig. 4. (a) Schematic of a waving plate and its wake. (b) Propulsive efficiency as a function of the reduced frequency. (c) Thrust coefficient as a function of the reduced frequency. (d) Power coefficient as a function of the reduced frequency. The solid lines represent the theory while the markers represent the computations. The triangle and square markers denote the small and large amplitudes of motion, respectively. The line and marker colors go from black to white to specify the wavenumbers from low to high values.

the theory. This is likely due to the numerical solutions using a small, finite thickness airfoil and small, but not infinitesimal amplitudes of motion. The theory and numerical solutions show that the thrust and power coefficient increase with increasing amplitude, however, the efficiency is independent of the amplitude of motion. In fact, the efficiency is only a function of the reduced frequency and wavenumber with higher wavenumbers being more efficient for a fixed reduced frequency. This is true as long as the thrust remains positive. Although it is not obvious in Fig. 4(c), the thrust switches to drag when $k < k_x$, which is evident from the theory. This comparison validates the accuracy of the current BEM formulation in modeling fully prescribed deforming bodies.

3.4. Three-Dimensional steady flow

The steady flow over a three-dimensional elliptical wing was examined to help validate the three-dimensional aspects of the current formulation. Prandtl's classic lifting line theory for elliptical wings solves this problem analytically [30]. This solution assumes that the wing is immersed in an incompressible, irrotational, and inviscid potential flow and that it can be modeled as a lifting bound vortex line and a shed vortex sheet that is planar and non-deforming. The theory further assumes that the wing is infinitesimally thin, at small angles of attack, and that while the wing is finite, the aspect ratio is high. To simulate the assumptions of the theory, a teardrop shaped airfoil with a maximum thickness-to-chord ratio of $t/c = 0.02$ was used to simulate a flat plate. A 2% thickness was chosen to be as thin as possible, but sufficiently thick so that there is a well-defined leading-edge in order to avoid numerical sensitivity in the induced drag calculation. There were 70 chordwise elements on the top and bottom surfaces as well as 50 spanwise elements for a total of 7000 body elements. The computation used 4 timesteps with $\Delta t = 250$ s. The freestream velocity and root chord length are $U_\infty = 1$ m/s and $c = 1$ m, respectively. A non-deforming wake was used in the force calculations of this validation. Fig. 5(a) and (b) presents the lift coefficient and the induced drag coefficient, respectively, for four different aspect ratios, that is, $AR = 5$, 10, 15, and 20. The numerical solutions are represented by the circle markers while the analytical solutions are represented by the solid lines. There is good agreement between the analytical and numerical calculations. Based on the assumptions of lifting line theory it is expected that the numerical and analytical solutions would deviate for the lower aspect ratios of $AR = 5$ and 10. An example of the wake structure for a deforming wake simulation is shown in Fig. 5(c). In this example the wing has an aspect ratio of $AR = 5$ and an angle of attack of $\alpha = 15^\circ$. The airfoil thickness-to-chord ratio is $t/c = 0.2$ to more clearly observe the pressure distribution. There are 70 timesteps with $\Delta t = 0.07$ s between them. At $t = 4.9$ s the wake shows a characteristic horseshoe vortex system connecting the tip vortices to the starting vortex. On the body the colormap represents the pressure coefficient. There is stagnation pressure near the leading and trailing-edges while there is a pressure minimum on the upper surface near the leading-edge responsible for leading-edge suction and a majority of the lift production.

3.5. Three-dimensional unsteady flow

The unsteady flow problem of the lift on an oscillating three-dimensional wing is examined next. There is a numerical solution to this problem presented by Katz [23] where he calculated the lift generated by a heaving three-dimensional rectangular wing at a negative angle of incidence using a boundary element method. For this case the rectangular wing has an aspect ratio of $AR = 4$, an angle of incidence $\alpha = -5^\circ$ and a heave amplitude of $h = 0.1$ c, where $c = 1$ m is the chord length. The reduced frequency $k = \pi f c/U_\infty$ is varied for three cases $k = 0.1$, 0.3, and 0.5 where f is the oscillation frequency, $T = 1/f$ is the period of motion, and $U_\infty = 1$ m/s is the free-stream velocity. In the current numerical implementation a 2% thick tear-drop shaped airfoil is used to simulate an infinitesimally-thin flat plate. A 2% thickness was chosen to be as thin as possible, but sufficiently thick so that there is a

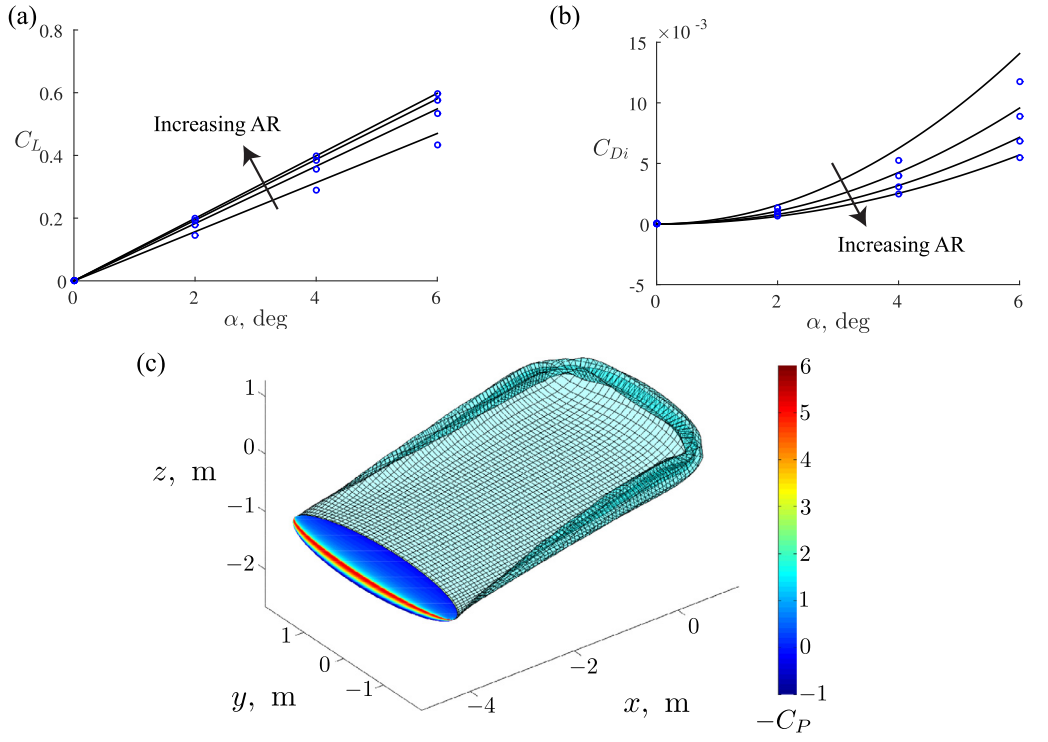

Fig. 5. Calculated (a) lift coefficient and (b) induced drag coefficient of steady flow over an elliptical wing at varying angles of attack, α. The numerical solution is denoted by the circle markers while the analytical solution is denoted by the solid lines. There are four aspect ratios used in the calculations: $AR = 5$, 10, 15, and 20. (c) Deforming wake solution at $t = 4.9$ s for the $AR = 5$, $\alpha = 15^\circ$.

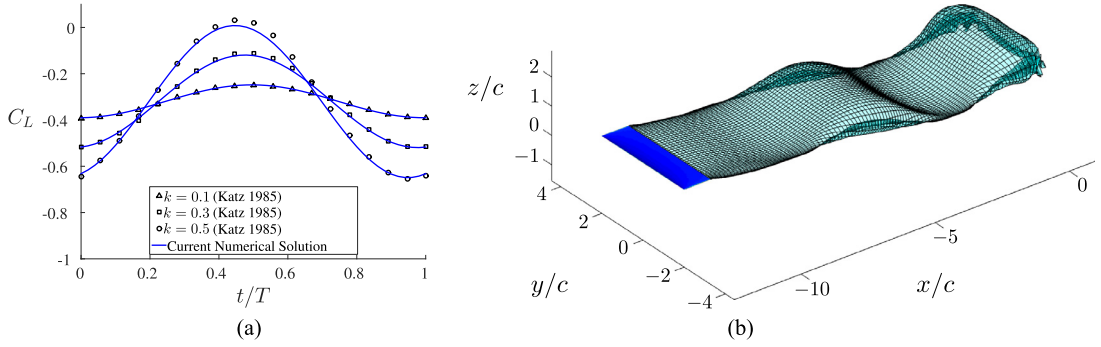

Fig. 6. Wing oscillating under unsteady flow conditions. (a) Lift coefficient calculated with the current numerical method (solid lines) compared to a previous numerical calculation (open markers) by Katz [23] for $k = 0.1$, 0.3, and 0.5. (b) Boundary element wake deformation for $k = 0.5$ and $t = 12.5$ s.

well-defined leading-edge in order to avoid numerical sensitivity in the force calculations. The top and bottom surface of the wing is discretized into 30 chordwise and 50 spanwise elements for a total of 3000 body elements. The computation is discretized into 50 timesteps per cycle with $\Delta t = [0.63, 0.21, 0.125]$ s for each of the reduced frequency cases respectively. A total of 4 oscillating cycles are computed. Fig. 6(a) shows the lift coefficient as a function of time over the fourth oscillation cycle. Excellent agreement can be seen between the current numerical implementation (solid line) and the numerical solution of [23] (open markers). As the reduced frequency is increased the magnitude of the unsteady lift is seen to grow and there is a negative phase-shift in the lift oscillation as well. Fig. 6(b) shows the rollup of the wake elements that are free to advect with the local velocity field for the case where $k = 0.5$ and at $t = 12.5$ s. As the airfoil heaves upward, the circulation from the unsteady motion adds to the circulation due to the angle of incidence and subsequently the tip vortices increase their strength. When the airfoil heaves downward the circulation due to the incidence angle and the downward motion counteract each other to produce weak tip vortices. The net effect is to produce oscillating regions of strong and weak upwash.

3.6. Viscous boundary layer solution

The viscous drag over a NACA 0012 airfoil was examined next by using the viscous boundary layer solver coupled with the outer potential flow solution from the boundary element method. Fig. 7(a) shows a wing with $AR = 4$ at an angle of attack $\alpha = 3^\circ$ and a Reynolds number of $Re = 1 \times 10^6$. The boundary elements are colored with the value for the shear stress acting on each element. When the wing is examined up close, the shear stress is seen to be high at the minimum pressure location on the wing as flow is accelerated around the leading-edge. Then the shear stress decreases downstream of the minimum pressure point until the boundary layer transitions to a turbulent boundary layer. At this location, the shear stress is seen to discontinuously increase and then slowly decrease toward the trailing edge.

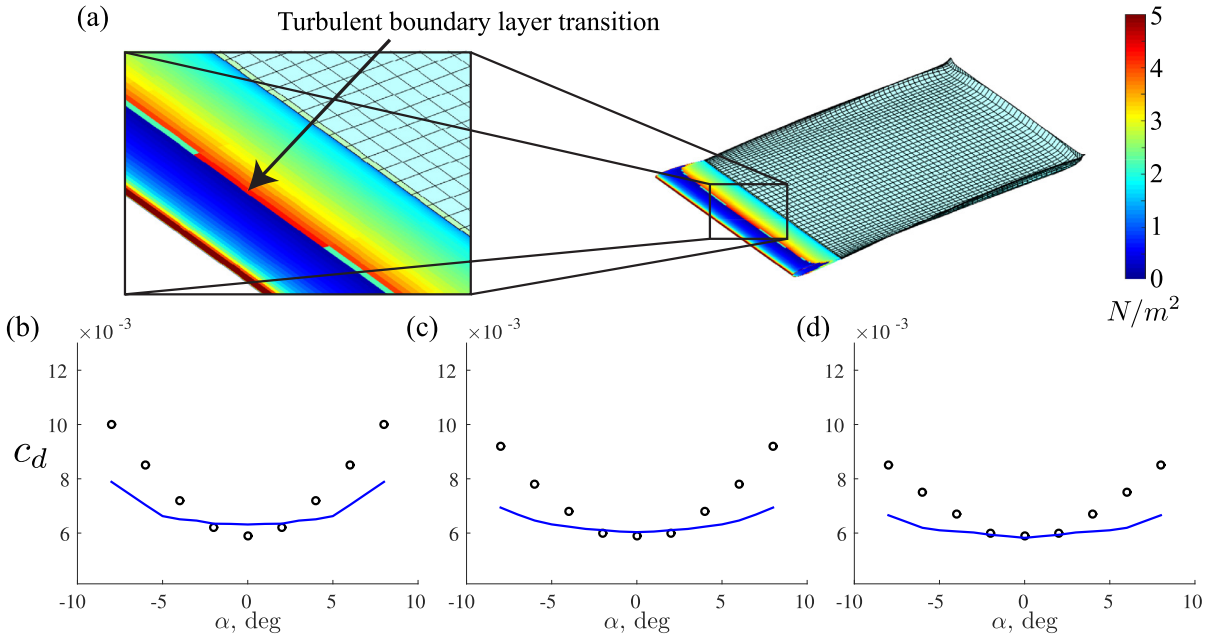

Fig. 7. (a) Shear stress on the surface of a NACA 0012 wing in steady flow conditions. Drag coefficient calculated numerically (solid line) compared to experimental data (circles) from Abbott and von Doenhoff [1]: (b) $Re = 3 \times 10^6$, (c) $Re = 6 \times 10^6$, and (d) $Re = 9 \times 10^6$.

A wing with an $AR = 1000$ was used to compare the calculated drag with experimental measurements published in Abbott and von Doenhoff [1]. The calculations spanned a range of angles of attack between -8° and 8° and three Reynolds numbers of $Re = [3 \times 10^6,\ 6 \times 10^6,\ 9 \times 10^6]$. The top and bottom surface of the wing is discretized into 50 chordwise and 50 spanwise elements for a total of 5000 body elements. The computation is discretized into 5 timesteps with $\Delta t = 200$ s. The wake is non-deforming in the computations.

Good agreement can be seen between the calculated drag coefficient (solid line) and the experimentally measured values (open circles) for low angles of attack less than $\pm 4^\circ$ where the calculated values are within 10% of the experimental values. For higher angles of attack, the drag coefficient is under-predicted by the numerical solution. In the worst case examined here the calculated drag is 22% lower than the measured value at $\alpha = 8^\circ$. This discrepancy is likely due to the approximate closure relation used in the boundary layer solver (see Section 2.9), which can be improved with entrainment relations [8]. Future work of incorporating a separation model may further improve the drag calculations. However, in many fish swimming applications the bodies of swimmers, typically the main drag contributor, have small amplitudes of motion and subsequently small local angles of attack making the current skin friction solver sufficient for many bio-inspired swimming calculations.

3.7. Self-propelled biological propulsion

Recent work has examined in detail the forces and flow structures exhibited by a numerical manta ray swimmer by using the code presented in the current study [16]. In the previous work the numerical method was not shown to be extensively validated as is the case and the focus of the current work. From extensive biological data gathered in aquaria and in the field, the manta ray swimmer (Fig. 8(a)) was modeled to be geometrically similar to real mantas and to oscillate its fins with the same kinematic motions of the rays (see [16] for further details). The swimming motions of the manta are three-dimensionally complex because of the flexibility of the propulsive pectoral fins. The manta propels itself by vertically moving its enlarged pectoral fins in a flapping motion, combined with waves moving through the fins in both the spanwise and chordwise directions. The motion is thus both oscillatory, and shape-changing (undulatory), although the undulatory component in the chordwise direction is small (the wavelength of the undulation is greater than the chord length of the pectoral fin).

Fig. 8(a) shows the vortex wake produced by a free-swimming manta ray. The vortices are marked as isosurfaces of the λ_2 criteria, which distinguishes pressure minima in a plane after discarding unsteady straining and viscous effects [21]. The manta is seen to shed a series of interlocked vortex rings with one set originating from each pectoral fin.

The left axis line in Fig. 8(b) shows the mean swimming speed normalized by the body length as a function of oscillation frequency for the numerical manta ray. The right axis line further normalizes the mean speed by the oscillation frequency to highlight the near linear dependence upon the oscillation frequency. The small blue points represent biological data of the swimming speed of real manta rays as a function of their oscillation frequency. Importantly, the present numerical method shows excellent agreement with the biological data indicating that the current method can predict the performance of real biological self-propelled swimmers.

4. Results

To investigate the capabilities and limitations of the current BEM implementation in predicting the self-propelled performance and wake structure of a bio-inspired device, the undulatory elliptical fin experiments of Moored et al. [31] are modeled. In these experiments a fin having an elliptical planform with an aspect ratio $AR = 1.6$ and a NACA 0020 cross-section was fabricated. The root chord length of the fin was $c = 0.254$ m. The fin had four actuating spars that were embedded into a PVC polymer and were actuated in such a manner as to produce a chordwise traveling wave (see [31] for the experimental details). The ratio of the traveling-wave wavelength to root chord in the experiments was varied from $\lambda/c = 3 - 12$. In the computations, the two cases of $\lambda/c = 6$ and 12 were modeled where $\lambda/c = 6$ was previously found to be the most

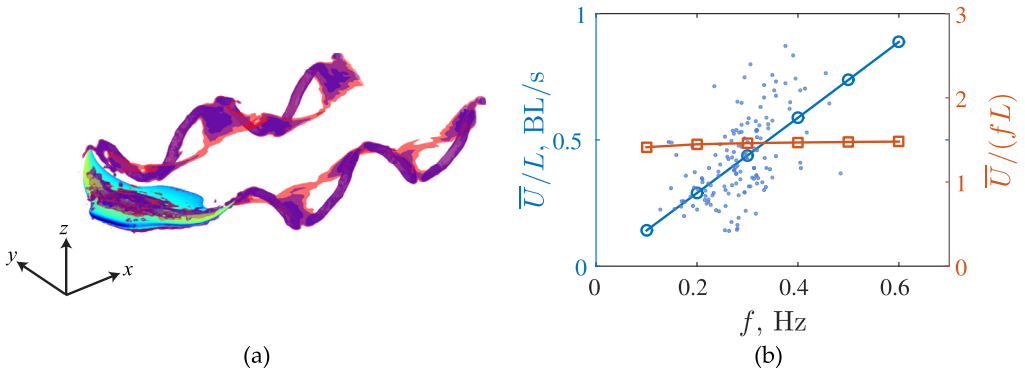

Fig. 8. Reproduced from [16]. (a) Vortex wake of a manta ray swimmer identified by isosurfaces of the λ_2 criteria. (b) Numerical calculations of the self-propelled speed as a function of frequency (solid lines with open markers) compared to biological data (filled markers). The left vertical axis shows the mean speed normalized by the body length while the right vertical axis shows the mean speed normalized by the frequency and body length.

Table 1
Simulation parameters used in the present study and experimental parameters used in [31]. Here, the wavenumber is based on the root chord length as $k_x = \pi c_r/\lambda$.

	Plate drag	Carriage friction	A (m)	λ/c	k_x
Experiments	Yes	Yes	0.025	6	0.52
Numerical case 1	Yes	Yes	0.025	6	0.52
Numerical case 2	No	No	0.025	6	0.52
Numerical case 3	No	No	0.025	12	0.26
Numerical case 4	No	No	0.05	6	0.52

efficient case [10,32]. The fin had a linearly increasing amplitude from root to tip in the spanwise direction with a peak-to-peak tip amplitude of $A_{pp} = 0.05$ m. The detailed kinematics of the fin motion are,

$$x = x_f \tag{45}$$

$$y = y_f \cos\left[\theta_{\max} g(t)\right] \tag{46}$$

$$z = y_f \sin\left[\theta_{\max} g(t)\right] \tag{47}$$

where:

$$g(t) = \sin\left(\omega t - k_x^* x_f/s\right), \quad \theta_{\max} = \sin^{-1}\left(\frac{A_{pp}}{2s}\right), \quad \omega = 2\pi f,$$

$$k_x^* = \frac{2\pi s}{\lambda}. \tag{48}$$

The x and y positions of neutral plane of the fin in a flat position are x_f and y_f, respectively. The oscillation frequency is f, the span length is s, the maximum rolling angle of the fin is $\theta_{\max}$, and the wavenumber based on the span length is k_x^*. The computational model of the undulatory fin can be seen in Fig. 10(a). The experimental fin was placed into a free-swimming water tank facility where it was attached to a carriage that was supported by low-friction carts on a rail system (Article No.: ME-9454; PASCO scientific). This setup allowed for unconstrained motion in the streamwise direction. The root of the fin was located at the free-surface where an acrylic plate was placed to dampen free-surface waves generated by the unsteady undulations of the fin.

To properly model this experiment several details must be considered. The free-surface and acrylic plate introduce a no-flux boundary condition that is modeled by using a mirror image fin connected at the root section. At the same time, the free-surface can produce waves from the streamwise motion of the plate, however, the wave drag from this motion is neglected in the computations. The acrylic plate though has another drag source, that is, skin friction drag from the production of its boundary layer. In the computations, the plate geometry is modeled such that the boundary layer solver calculates the skin friction drag from the plate as well as the submerged body. The forces acting on the mirror image body and mirror image plate are neglected in the free-swimming calculations. The low-friction carts actually have a finite rolling friction coefficient, which has been measured to be $\mu_r = 0.0065 \pm 0.0002$ [34]. The friction coefficient was found to be relatively independent of the speed, that is, it changed by less than 10% for speeds between 0 and 2 m/s. This speed range covers the swimming speeds attained during the experiment, so the friction force resisting the motion, $F_{fr} = \mu_r W$, where W is the net weight of carriage fin system. This rolling frictional force was included in some of the computations. The PVC polymer used to fabricate the fin is less dense than water and produces a buoyant force that counteracts the dry weight of the carriage and fin. The net weight of the whole system when the fin is submerged is estimated at $W \approx 15$ N.

4.1. Self-propelled performance metrics

There are several self-propelled performance metrics that are reported in this study. Time-averaged quantities are marked by an overbar and are always averaged over the last cycle of the computations. The time-averaged thrust coefficient, net thrust coefficient and power coefficient are defined as

$$C_T = \frac{\overline{T}}{1/2\,\rho \overline{U}^2 S}, \quad C_{T,net} = \frac{\overline{T}_{net}}{1/2\,\rho \overline{U}^2 S}, \quad C_P = \frac{\overline{P}}{1/2\,\rho \overline{U}^3 S}, \tag{49}$$

respectively. The time-averaged swimming speed is $\overline{U}$, the time-averaged power input to the fluid is $\overline{P}$, the planform area is S and the fluid density is ρ. The time-averaged thrust force, $\overline{T}$, is the streamwise component of the force from pressure forces alone and the force is considered positive when it is acting on the body in the $-x$ direction. The time-averaged net thrust force, $\overline{T}_{net}$, is the difference between the thrust force and the total drag force, which includes all of the sources of drag that are present in a given computation, that is, the skin friction drag over the fin and the wave-suppression plate, and the rolling friction drag of the rail-carriage system.

In addition, the Strouhal number, reduced frequency, non-dimensional speed, propulsive efficiency and the swimming economy are reported as

$$St = \frac{fA}{\overline{U}}, \quad k = \frac{\pi f c}{\overline{U}}, \quad U^* = \frac{\overline{U}}{fc}, \quad \eta = \frac{\overline{T}\overline{U}}{\overline{P}}, \quad \xi = \frac{\overline{U}}{\overline{P}}, \tag{50}$$

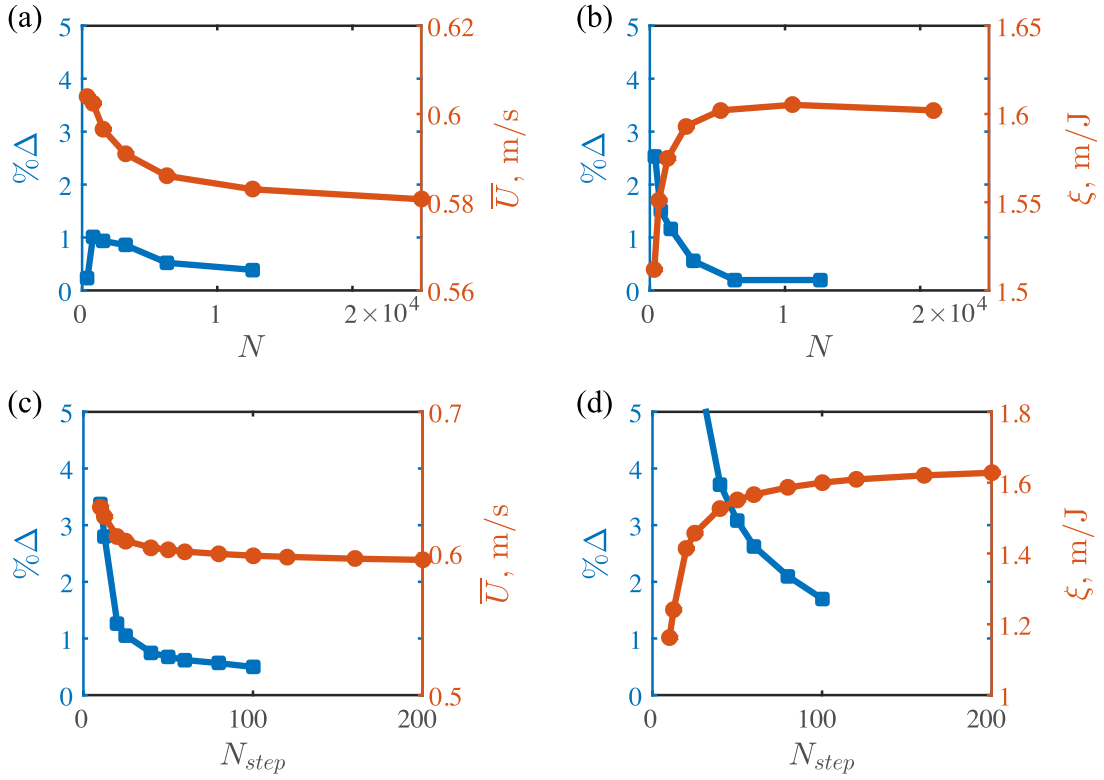

Fig. 9. Right axes: convergence of the time-averaged swimming speed and the swimming economy for varying numbers of the body elements and time steps per oscillation cycle. Left axes: percent change (%Δ) in the swimming speed or economy when the number of body elements or time steps per cycle are doubled. For (a) and (b), the number of time steps per oscillation cycle is fixed at $N_{step} = 50$. For (c) and (d), the number of body elements is fixed at $N = 800$.

respectively, where the frequency of oscillation is f, the tip amplitude is $A = A_{pp}/2$ and $\overline{TU}$ is the time-averaged useful power output. The non-dimensional speed, U^*, represents the distance traveled in chord lengths over a period of oscillation and is effectively the inverse of the reduced frequency. The propulsive efficiency is the ratio of useful power output to power input, while the swimming economy represents the distance that can be traveled with a unit of energy. Both energetic swimming metrics are reported since the economy is more readily measured in self-propelled swimming experiments, while the efficiency is non-dimensional and easily comparable between different systems.

4.2. Discretization independence

Convergence of the time-averaged swimming speed, $\overline{U}$, and the swimming economy, ξ, was tracked as the number of body elements and the number of time steps per oscillation cycle were varied (Fig. 9). The convergence computations are executed for 3 oscillation cycles. On the right axes in Fig. 9, good convergence of the swimming speed and swimming economy are shown for both variations in the number of body elements and the number of time steps per oscillation cycle. The left axes show the percent change (%Δ) in either the swimming speed or economy when the number of body elements or time steps per cycle are doubled. It is determined that the free-swimming solution changes by $\mathcal{O}(1\%)$ when $N = 3200$[1] is doubled and by $\mathcal{O}(2\%)$ when $N_{step} = 80$ is doubled. These values for N and N_{step} are fixed for all of the following results.

[1] More specifically, there are 40 chordwise elements for the top surface, 40 chordwise elements for the bottom surface and 40 spanwise elements for the combined body of the fin and its image

4.3. Pectoral fin locomotion

The self-propelled performance of an undulating elliptical fin is examined in detail to offer a direct comparison of the self-propelled three-dimensional unsteady boundary element implementation formulated in this study with previously published experimental data. Additionally, the self-propelled performance of other cases that *extend beyond* the previous experiments are examined to provide novel physical insight into the self-propulsion of three-dimensional bio-inspired ray-like fins.

Rays have dorso-ventrally flattened bodies with enlarged pectoral fins that they use to propel themselves through the water [12,17,18,26]. They employ a kinematic motion that is a combination of large-amplitude flapping with spanwise curvature and a chordwise traveling-wave motion [33]. Based on their kinematics, rays have been classified along an undulation-oscillation continuum characterized by their non-dimensional wavelength of motion [44]. Undulatory motion defined as having greater than one wave present on a fin [42] was termed 'rajiform' [7] while 'mobuliform' or oscillatory motions have less than half of a wave present on a fin [51]. In recent years not only have biologists studied the form and function of ray-like motions, but also engineers have examined rays as an ideal platform to mimic in the design of bio-inspired underwater vehicles [43]. For the next-generation of these vehicles, improvements in speed and efficiency are highly desired and the chordwise traveling-wave component of the fin motions has been identified as a key feature to attain high-efficiency swimming [31]. In fact, the chordwise traveling motion of rays has been directly examined by a bio-robotic fin at a *fixed-velocity* in a flow channel with direct force measurements and dye flow visualization to track shed vortex structures [10]. In these experiments, the Strouhal number and the non-dimensional wavelength were varied leading to a peak efficiency of 55%. However, the experi-

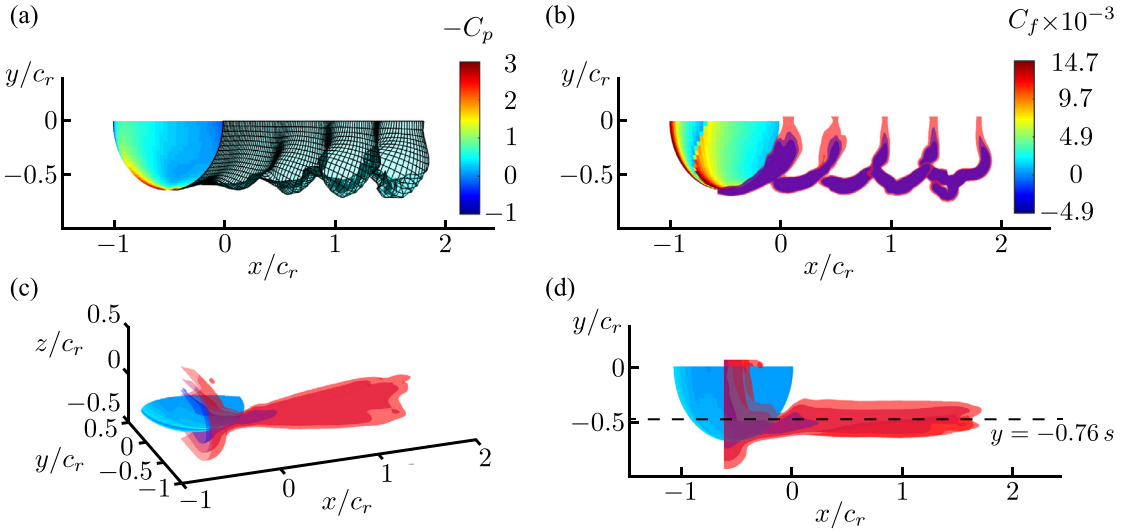

Fig. 10. Numerical case 1 (Table 1) where $f = 2$ Hz and $t = 1.5$ s when the initial velocity condition is the steady-state swimming speed. (a) Boundary element discretization of the wake. The fin surface colormap represents the pressure coefficient. (b) Vortex wake identified by isosurfaces of the λ_2 criteria. The fin surface colormap represents the skin friction coefficient. (c) and (d) Isosurfaces of the time-averaged x-component of the velocity. The pink, red and purple isosurfaces are 5%, 7% and 10% above the mean swimming speed. (For interpretation of the references to color in this figure legend, the reader is referred to the web version of this article.)

ments were not self-propelled and only one non-dimensional amplitude of motion was considered, which was a factor of 2–3 times smaller than that observed in the freshwater stingray [4]. Dewey et al. [11] further quantified the three-dimensional wake structures of an experimental undulating fin and determined that for inefficient motions bifurcating momentum jets formed in the near wake of the fin. More recently, three-dimensional fin kinematics data of the freshwater stingray have been acquired [4] and used in conjunction with self-propelled CFD simulations to determine that a leading-edge vortex forms and improves the swimming efficiency of stingrays [6].

Considering this work, the current study uses the newly developed boundary element formulation to extend this previous work in several directions. Instead of using the exact geometry and kinematics of rays as in the self-propelled CFD work of [6], here an idealized undulating elliptical fin will be used to systematically probe the effect of *independent wavenumber and amplitude variations* on self-propelled swimming. The model follows the geometry and kinematics of [10,11,31], however, these studies are extended by considering the effect of amplitude variation on an undulating fin in a self-propelled swimming state. Finally, under these conditions the performance of the fin is connected to the momentum jet formation in its near wake.

4.4. Wake structure and self-propelled performance

The simulation parameters used for the four numerical cases and the previous experiment data [31] are summarized in Table 1. The first numerical case models the exact experimental conditions and parameters used in [31]. Numerical cases 2–4 examine different parameter combinations of amplitude, A, and nondimensional wavelength, λ/c, under no plate drag and no carriage friction conditions. Plate drag and carriage friction were necessary conditions imposed by the experimental apparatus, however, these conditions are not present in a self-propelled bio-inspired device. By eliminating these conditions in the numerical simulations, the actual performance of a self-propelled fin can be directly examined. The fin simulations were seeded with initial speeds close to the experimental values and a simulation was run for six cycles. Then to quickly converge to a solution, the steady-state mean speed was estimated and another six cycles were run with the estimate as the initial condition. These guess-and-check iterations limited long simulations, which was important since the mass of the experiment was large and the fin's streamwise accelerations were quite low, otherwise leading to excessively long simulations. All of the self-propelled simulations have reached a steady-state condition, that is, the number of oscillation cycles was increased until the cycle-averaged net thrust coefficient was $C_{T,net} = \mathcal{O}(10^{-4})$.

Fig. 10 presents the wake structure of the ellipitcal bio-inspired fin for numerical case 1 (see Table 1) with $f = 2$ Hz. Fig. 10(a) shows the wake doublet elements rolling up into coherent vortex structures, which is made evident with the λ_2 isosurfaces highlighted in Fig. 10b. It is clear that the elliptical fin is shedding a series of interlocked vortex rings through which fluid is accelerated. In fact, the time-average of the streamwise velocity is shown for isosurfaces of 5%, 7% and 10% above the free-stream velocity for the pink, red and purple surfaces, respectively (Fig. 10(c) and (d)). Note that the isosurface calculation begins at nearly the half-chord of the fin. The time-averaged jet of fluid accelerated by the vortex rings is observed to have its peak momentum flux at 76% of the span (Fig. 10(d)). This is in good agreement with previous experiments [11] that found the peak momentum flux to occur at about 80% of the span. The surface of the fin is colored with the pressure coefficient in Fig. 10(a), which is defined as $C_p = P/\left(1/2\,\rho\overline{U}^2\right)$. The pressure distribution shows a clear leading-edge suction signature occurring near the fin tip that is coincident with the region of the highest momentum flux generated by the fin. The shear stress distribution computed from the boundary layer solver is shown on the surface of the fin in Fig. 10(b) and is nondimensionalized as a skin friction coefficient, that is $C_f = \tau/\left(1/2\,\rho\overline{U}^2\right)$. High shear stress can be seen near the leading edge where the flow is accelerated, but the boundary layer remains laminar. The shear stress rises to high values near the quarter-chord of the fin due to a transition in the boundary layer to turbulence. This indicates that a majority of the skin friction acting on the fin is coming from a turbulent boundary layer. All of the other cases show the same salient features of the wake as well as the pressure and shear stress distributions.

Although all of the cases produce time-averaged momentum jets, the structure of the momentum jets are quite different. Fig. 11 presents the time-averaged streamwise and cross-stream velocities

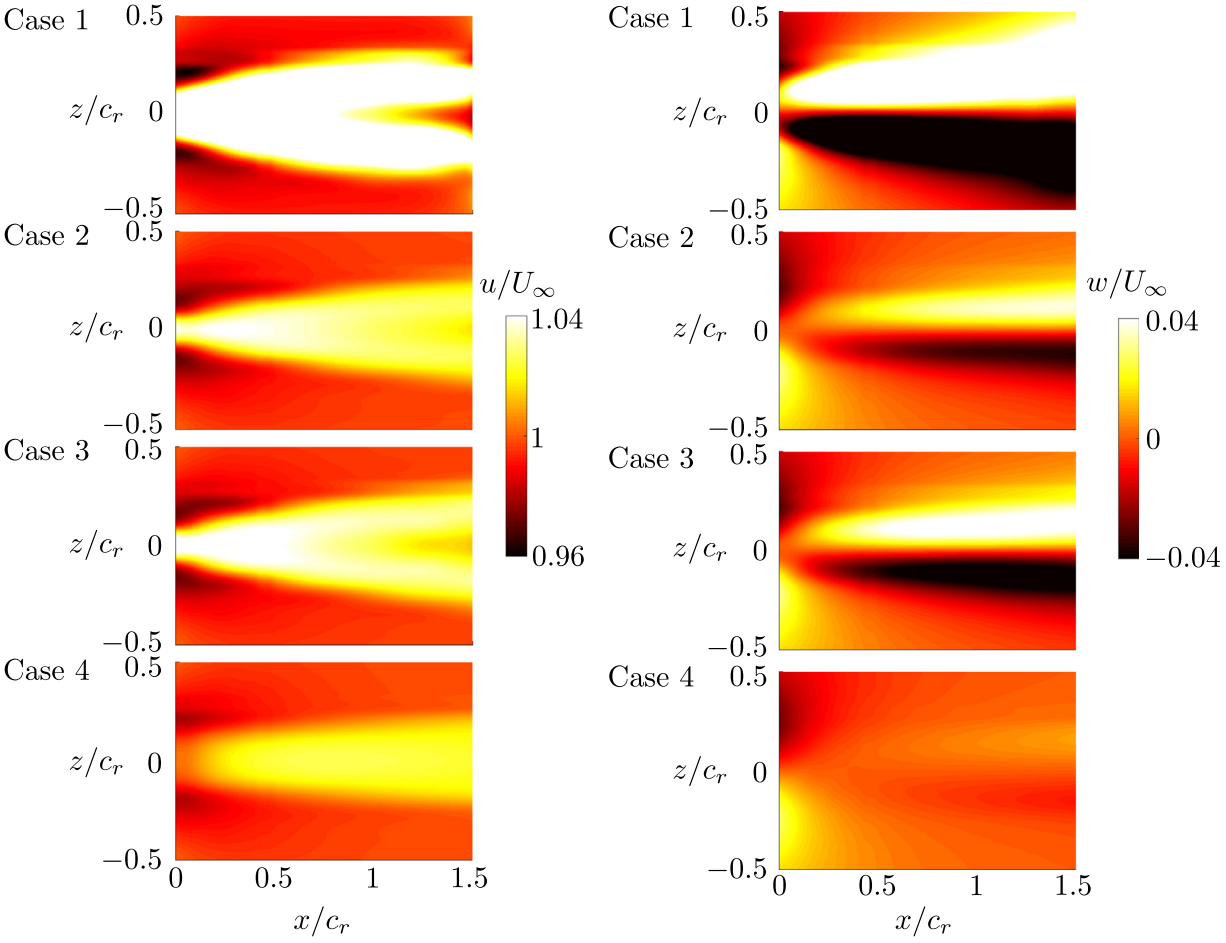

Fig. 11. Time-averaged x-velocity (left) and z-velocity (right) in an $x - z$ plane at 76% of the span for the four numerical cases.

in the $x - z$ plane that cuts through the core of momentum jets at 76% of the span for all four numerical cases. The mean streamwise velocity for cases 1–3 show bifurcating jets where the jet splits into two branches. Bifurcating jets have been implicated in poor efficiency performance [11,13]. In fact, the time-averaged lateral velocity (Fig. 11 right) highlights that there is excess lateral momentum such that some of the momentum added to the fluid does not perform useful work. In contrast, case 4 shows a single, non-bifurcating momentum jet and minute amounts of excess lateral momentum. By considering the magnitude of the lateral momentum relative to the streamwise momentum, the efficiency of each case could be predicted to be ordered from the least efficient to the most efficient as case 1, 3, 2 and 4, respectively. Indeed, as can be observed later in Fig. 13 this is exactly the ordering of the cases based on their efficiency. It can be further observed that as the wavenumber on the fin decreases the jet bifurcation moves closer to the trailing edge as seen in [11]. Additionally, a *key insight* is that case 4 has twice the amplitude of motion of the other cases, which consequently leads to the suppression of the jet bifurcation and in turn high efficiency locomotion.

Fig. 12(a) presents the self-propelled swimming speed of the elliptical fin for a range of frequencies of $f = 1.2 - 2$ Hz. The experimental data [31] shows that the swimming speed of the undulating fin increases nearly linearly with an increasing frequency of motion. Similarly, the numerical simulations show a nearly linearly increasing swimming speed with increasing frequency, however, with a slightly lower slope. Regardless of this discrepancy, there is still excellent agreement between the numerical simulations and the experimental data further validating the self-propelled numerical implementation presented in this study. It is expected that viscous effects in the experiments such as small regions of separated flow near the trailing-edge, the three-dimensional boundary layers, or boundary layer thinning from the unsteady motions [14,15] can account for the differences among these data. As expected, when the experimental conditions of plate drag and carriage friction are eliminated (cases 2–4) the undulating fin is observed to have a higher self-propelled swimming speed than case 1 at the same frequency of motion (Fig. 12(a)). When the nondimensional wavelength of motion is doubled from $\lambda/c = 6$ to $\lambda/c = 12$ there is a slight increase in the slope of the swimming speed curve, but otherwise a negligible effect on the swimming speed. However, another *key insight* is that when the amplitude of motion is doubled from $A = 0.025$ m to $A = 0.05$ m, the swimming speed is nearly doubled for all frequencies examined (percent increase of 93–97%).

Fig. 12(b) presents the Strouhal number as a function of the swimming speed. Again, the numerical data (case 1) is observed to show excellent agreement with the experimentally measured Strouhal number and both curves show decreasing St with an increase in the frequency of motion and in turn the swimming speed. Cases 2–4 exhibit a nearly constant St, however, they show a slightly decreasing trend with an increase in the swimming speed. In fact for cases 2–4 the swimming speed does indeed increase proportionally with the frequency leading to a nearly constant St. In contrast, the additional friction from the carriage and additional drag from the plate modify the swimming speed to be a nonlinear function of the frequency that is not obvious in Fig. 12(a), but is made evident by the nonlinear relationship between the St and the swimming speed.

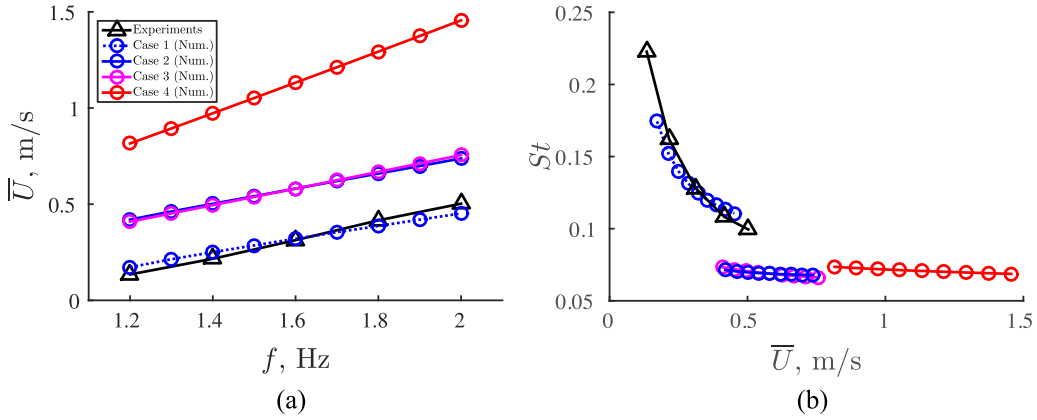

Fig. 12. (a) Self-propelled swimming speed as a function of frequency. (b) Strouhal number as a function of self-propelled swimming speed. All subsequent experimental and numerical cases marker and line styles follow the legend in (a).

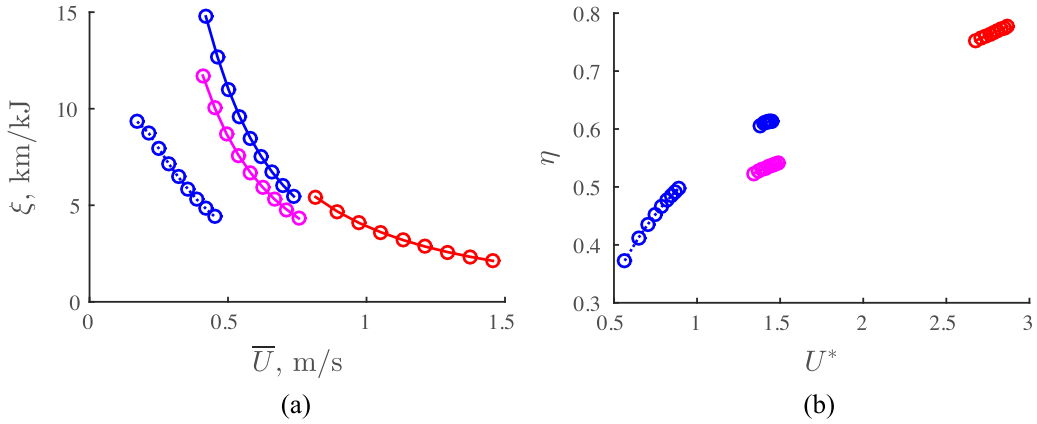

Fig. 13. (a) Swimming economy as a function of the self-propelled swimming speed. (b) Propulsive efficiency as a function of the nondimensional swimming speed.

Fig. 13a presents the swimming economy as a function of the swimming speed. For all cases, as the swimming speed increases there is an inverse relationship with the economy, that is, when swimming faster the distance that can be travelled for a unit of energy is smaller. This trend has been observed in the self-propelled swimming of manta rays [16] and in the self-propelled swimming of heaving flexible panels [38]. However, this trend contradicts the measurements of swimming economy observed in [31] and indicates that there was likely an error in those power measurements given the excellent agreement in swimming speed between the numerics and experiments. Intuitively, one would expect the economy to, in general, have an inverse trend with swimming speed as observed in the current study since the reverse would imply that it would take little energy to swim a given distance for the fastest swimming speeds, which seems unlikely. To support this intuition, when the economy relationship is examined,

$$\xi = \frac{\overline{U}}{\overline{P}} = \frac{1}{1/2\,\rho \overline{U}^2 S}\left(\frac{1}{C_P}\right), \tag{51}$$

it can be observed that the economy has an inverse relationship with the swimming speed and the power coefficient, which is also a function of the swimming speed. Furthermore, experimental power measurements have been reported in [10] for the same undulating fin as in [31], except that the fin was held in a water channel at a fixed velocity instead of operating in a self-propelled swimming state. If these power measurements are comparable, then [10] indicates a 5 fold drop in power when the Strouhal number drops from $St = 0.225$ to $St = 0.1$, precisely the St range observed in [31] that in turn corresponds to the speed range of $0.134 \le \overline{U} \le 0.503$. Now, the highest speed, $\overline{U}_H$, in [31] relates to the lowest speed, $\overline{U}_L$, as $\overline{U}_H = 3.75\,\overline{U}_L$ and the subsequent power coefficients are related by $C_{P,H} = 1/5\,C_{P,L}$. By forming a ratio of the economy at the highest swimming speed with the economy at the lowest swimming speed the trend in the economy can be estimated as,

$$\mathcal{R} = \frac{\xi_H}{\xi_L} = \frac{\overline{U}_L^2 C_{P,L}}{\overline{U}_H^2 C_{P,H}} = \frac{5}{3.75^2} = 0.3556 \tag{52}$$

When the ratio $\mathcal{R} < 1$ the economy is estimated as having an inverse trend with swimming speed and when the $\mathcal{R} > 1$ *vice versa*. The ratio based on the previous power measurements from [10] is $\mathcal{R} = 0.3556$ estimating that the economy should drop by nearly one-third in the experiments over the tested speed range. This estimate further supports the findings of the current numerical study and the idea that the previous experiments have an error in their power measurements. In fact, the ratio of economies using the numerical data (case 1) from Fig. 13 is $\mathcal{R} = 0.4725$, which is in good agreement with the expected ratio of economies from the experiments.

Fig. 13(b) presents the propulsive efficiency as a function of the non-dimensional swimming speed. Even though the economy is low for the high swimming speeds and for the high amplitude case (case 4), the efficiency is the highest for these cases with a peak efficiency for case 4 of $\eta \approx 78\%$. A *key insight* is that high propulsive efficiency occurs when the amplitude of motion is doubled, which, during self-propelled swimming, leads to nearly twice the swimming speed and half of the reduced frequency ($k \equiv \pi/U^*$). Wu's waving plate theory [55] would predict that for

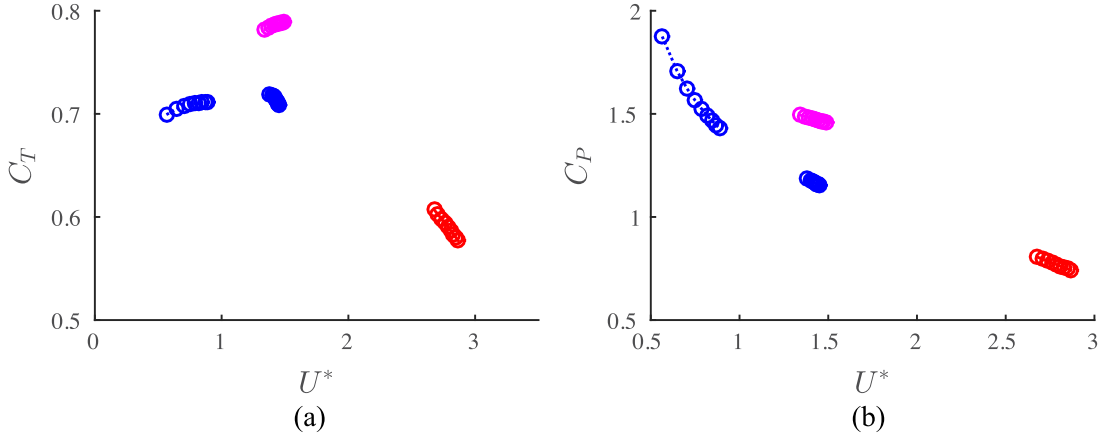

Fig. 14. (a) Thrust coefficient as a function of the nondimensional swimming speed. (b) Power coefficient as a function of the nondimensional swimming speed.

a fixed wavenumber the propulsive efficiency should increase as the reduced frequency decreases as observed in the present calculations. Also, the peak efficiency for case 1 is $\eta \approx 50\%$, which is in good agreement with the experimentally measured peak efficiency being $\eta \approx 55\%$ [10]. Interestingly, if the experiments were fully self-propelled without the additional plate drag and carriage friction the numerical results indicate that a peak efficiency of $\eta \approx 61\%$ could be attained. Now, it is also clear that even though the higher nondimensional wavelength ($\lambda/c = 12$, case 3) did not produce significantly different swimming speeds than case 2, it did reduce the propulsive efficiency to a peak value of $\eta \approx 54\%$. It can be noted that since the swimming speeds are effectively the same, so two are the reduced frequencies and Wu's waving plate theory [55] would predict a reduction in efficiency with a decrease in the wavenumber. This is precisely what is observed in Fig. 13(b).

The trends in propulsive efficiency can be further decomposed by examining the thrust (Fig. 14(a)) and power coefficients (Fig. 14b) since $\eta = C_T/C_P$. It is observed that the thrust coefficient for $\lambda/c = 12$ (case 3) is actually higher than $\lambda/c = 6$ (case 2) indicating that the swimming speed is not linearly proportional to changes in C_T, but instead is proportional to the frequency and amplitude of motion as proposed in [2]. It is clear though that the power coefficient rise is greater than the thrust coefficient rise leading to a lower efficiency. Additionally, the higher amplitude motion (case 4) is observed to slightly reduce the thrust coefficient as compared to case 2. At the same time the power is also significantly reduced leading to higher efficiency. Case 2 shows both a higher thrust coefficient and a lower power coefficient than case 1 leading to an increase the propulsive efficiency.

5. Conclusions

A novel boundary element method implementation is developed and presented to examine problems of biological and bio-inspired self-propelled locomotion. The formulation uniquely combines an unsteady three-dimensional boundary element fluid solver, a boundary layer solver and an equation of motion solver. The method is validated through a series of analytical, numerical and experimental data that include comparisons with two-dimensional and three-dimensional steady flow solutions, two-dimensional and three-dimensional unsteady flow solutions, viscous drag measurements, self-propelled biological field measurements and self-propelled bio-inspired laboratory measurements. The method is then employed to extend previous experimental results on a ray-inspired model of a self-propelled undulating fin. Based on the key insights of this study, the following framework can be concluded. For undulating fins a decrease in the wavenumber on the fin will have no significant effect on the swimming speed, but instead increase the power consumption and decreases the propulsive efficiency and *vice versa*. Additionally, as the wavenumber is decreased the bifurcation point of the momentum jet in the near wake will move closer to the fin also indicating decreased efficiency performance. In contrast, an increase in the amplitude of motion will proportionally increase the swimming speed, and consequently lower the reduced frequency. In accordance with Wu's waving plate theory [55], this will improve the propulsive efficiency. At the same time, the bifurcating momentum jet in the wake will be suppressed and a single core jet will be formed. This indicates improved efficiency performance as the wasted lateral momentum in the wake is minimized.

Acknowledgments

This work was supported by the Office of Naval Research under Program Director Dr. Robert Brizzolara, MURI grant number N00014-08-1-0642. I would like to acknowledge the helpful discussions with Dan Quinn and Peter Dewey on the design of the experimental undulating elliptical fin.

References

[1] Abbott IH, von Doenhoff AE. Theory of wing sections. Dover Publications; 1959.
[2] Bainbridge BYR. The speed of swimming of fish as related to size and to the frequency and amplitude of the tail beat. J Exp Biol 1957;35(1937):109–33.
[3] Basu BC, Hancock GJ. The unsteady motion of a two-dimensional aerofoil in incompressible inviscid flow. J Fluid Mech 1978;87(1):159–78.
[4] Blevins EL, Lauder GV. Rajiform locomotion: three-dimensional kinematics of the pectoral fin surface during swimming in the freshwater stingray potamotrygon orbignyi. J Exp Biol 2012;215(18):3231–41.
[5] Borazjani I, Ge L, Sotiropoulos F. Curvilinear immersed boundary method for simulating fluid structure interaction with complex 3d rigid bodies. J Comput Phys 2008;227(16):7587–620.
[6] Bottom RG, Borazjani I, Blevins EL, Lauder GV. Hydrodynamics of swimming in stingrays: numerical simulations and the role of the leading-edge vortex. J Fluid Mech 2016;788:407–43.
[7] Breder CM. The locomotion of fishes. Zoologica 1926;4:159–297.
[8] Cebeci T, Smith, A M O. Calculation of profile drag of airfoils at low mach numbers. J Aircr 1968;5(6).
[9] Cheng J, Chahine GL. Computational hydrodynamics of animal swimming: boundary element method and three-dimensional vortex wake structure. Comparat Biochem Physiol 2001;131:51–60.
[10] Clark RP, Smits aJ. Thrust production and wake structure of a batoid-inspired oscillating fin. J Fluid Mech 2006;562:415–29.
[11] Dewey PA, Carriou A, Smits AJ. On the relationship between efficiency and wake structure of a batoid-inspired oscillating fin. J Fluid Mech 2011;691:245–66.
[12] Santo VD, Blevins EL, Lauder GV. Batoid locomotion: effects of speed on pectoral fin deformation in the little skate, leucoraja erinacea. J Exp Biol 2017;220(4):705–12.
[13] Dong H, Mittal R, Bozkurttas M, Najjar F. Wake structure and performance of finite aspect-ratio flapping foils. 43rd AIAA aerospace sciences meeting and exhibit; 2005.

[14] Ehrenstein U, Eloy C. Skin friction on a moving wall and its implications for swimming animals. J Fluid Mech 2013;718:321–46.
[15] Ehrenstein U, Marquillie M, Eloy C. Skin friction on a flapping plate in uniform flow. Proc R Soc A 2014;372(2020):20130345.
[16] Fish FE, Schreiber CM, Moored KW, Liu G, Dong H, Bart-Smith H. Hydrodynamic performance of aquatic flapping: efficiency of underwater flight in the manta. Aerospace 2016;3(20):1–30.
[17] Fish FE, Hoffman JL. Stability design and response to waves by batoids. Integr Comp Biol 2015;55(4):648–61.
[18] Fontanella JE, Fish FE, Barchi EI, Campbell-Malone R, Nichols RH, DiNenno NK, Beneski JT. Two- and three-dimensional geometries of batoids in relation to locomotor mode. J Exp Mar Biol Ecol 2013;446:273–81.
[19] Haberman R. Applied partial differential equations: with Fourier series and boundary value problems. 4th. Pearson Prentice Hall, Upper Saddle River, NJ; 2004.
[20] Hess JL. Calculation of potential flow about arbitrary three-dimensional lifting bodies. Technical report. Douglas Aircraft Company, Long Beach, California; 1972.
[21] Jeong J, Hussain F. On the identification of a vortex. J Fluid Mech 1995;285:69–94.
[22] Kagami S, Fukai I. Application of boundary-element method to electromagnetic field problems. Microw Theory Tech IEEE Trans 1984;32(4):455–61.
[23] Katz J. Calculation of the aerodynamic forces on automotive lifting surfaces. ASME J Fluids Eng 1985;107:438–43.
[24] Katz J, Plotkin A. Low-speed aerodynamics. 2nd. Cambridge University Press, New York, NY; 2001.
[25] Krasny R. Desingularization of periodic vortex sheet roll-up. J Comput Phys 1986;65:292–313.
[26] Lauder GV, Santo VD. Swimming mechanisms and energetics of elasmobranch fishes. Fish Physiol Part A 2015;34:219–53.
[27] Liu P, Bose N. Propulsive performance from oscillating propulsors with spanwise flexibility. Proc R Soc A 1997;453:1763–70.
[28] Liu P, Bose N. Hydrodynamic characteristics of a lunate shape oscillating propulsor. Ocean Eng 1999;26:519–29.
[29] Maskew B. Program VSAERO theory document. Technical report. NASA CR-4023; 1987.
[30] Milne-Thomson LM. Theoretical aerodynamics. 4th. Dover Publications, New York, NY; 1958.
[31] Moored KW, Dewey PA, Leftwich MC, Bart-Smith H, Smits AJ. Bioinspired propulsion mechanisms based on manta ray locomotion. Mar Technol Soc J 2011;45(4):110–18.
[32] Moored KW, Dewey PA, Smits AJ, Haj-Hariri H. Hydrodynamic wake resonance as an underlying principle of efficient unsteady propulsion. J Fluid Mech 2012;708:329–48.
[33] Moored KW, Fish FE, Kemp TH, Bart-Smith H. Batoid fishes: inspiration for the next generation of underwater robots. Mar Technol Soc J 2011;45(4):99–109.
[34] Mungan CE. Rolling friction on a wheeled laboratory cart. Phys Educ 2012;47(3):288–92.
[35] Pan Y, Dong X, Zhu Q, Yue DKP. Boundary-element method for the prediction of performance of flapping foils with leading-edge separation. J Fluid Mech 2012;698:446–67.
[36] Portela A, Aliabadi MH, Rooke DP. The dual boundary element method: effective implementation for crack problems. Int J Numer Methods Eng 1992;33:1269–87.
[37] Pozrikidis C. Interfacial dynamics for stokes flow. J Comput Phys 2001;169(2):250–301.
[38] Quinn DB, Lauder GV, Smits AJ. Scaling the propulsive performance of heaving flexible panels. J Fluid Mech 2014;738:250–67.
[39] Quinn DB, Moored KW, Dewey PA, Smits AJ. Unsteady propulsion near a solid boundary. J Fluid Mech 2014;742:152–70.
[40] Ramesh K, Gopalarathnam A, Granlund K, Ol M, Edwards J. Discrete-vortex method with novel shedding criterion for unsteady aerofoil flows with intermittent leading-edge vortex shedding. J Fluid Mech 2014;751:500–38.
[41] Robinson DE. Implementation of a separated flow panel method for wall effects on finite swept wings. Ph.d. thesis. Massachusetts Institute of Technology; 1988.
[42] Rosenberger LJ. Pectoral fin locomotion in batoid fishes: undulation versus oscillation. J Exp Biol 2001;204:379–94.
[43] Russo RS, Blemker SS, Fish FE, Bart-Smith H. Biomechanical model of batoid (skates and rays) pectoral fins predicts the influence of skeletal structure on fin kinematics: implications for bio-inspired design. Bioinspir Biomim 2015;10(4):46002.
[44] Sfakiotakis M, Lane DM, Davies JBC, Bruce J, Davies C. Review of fish swimming modes for aquatic locomotion. IEEE J Oceanic Eng 1999;24(2):237–52.
[45] Shoele K, Zhu Q. Numerical simulation of a pectoral fin during labriform swimming. J Exp Biol 2010;213:2038–47.
[46] Shoele K, Zhu Q. Fluid-structure interactions of skeleton-reinforced fins: performance analysis of a paired fin in lift-based propulsion. J Exp Biol 2009;212:2679–90.
[47] Smith MJC. Simulating moth wing aerodynamics: towards the development of flapping-wing technology. AIAA J 1996;34(7):1348–55.
[48] Theodorsen T. General theory of aerodynamic instability and the mechanism of flutter. Technical report. NACA report No. 496; 1935.
[49] van de Vooren AI, de Jong LS. Calculation of incompressible flow about aerofoils using source, vortex and doublet distributions. Technical report. TW-86 of the Math. Inst. of the University of Groningen, The Netherlands; 1969.
[50] Voutsinas SG. Vortex methods in aeronautics: how to make things work. Int J Comut Fluid Dyn 2006;20(1):3–18.
[51] Webb PW. The biology of fish swimming. Mechanics and physiology of animal swimming 4562; 1994.
[52] White FM, Corfield I. Viscous fluid flow. 2nd. McGraw-Hill, New York; 2006.
[53] Willis DJ. An unsteady, accelerated, high order panel method with vortex particle wakes. Ph.d. thesis. Massachusetts Institute of Technology; 2006.
[54] Willis DJ, Peraire J, White JK. A combined pFFT-multipole tree code, unsteady panel method with vortex particle wakes. Int J Numer Methods Fluids 2007;53:1399–422.
[55] Wu TY-T. Swimming of a waving plate. J Fluid Mech 1960;10(3):321–44.
[56] Zhu Q. Numerical simulation of a flapping foil with chordwise or spanwise flexibility. AIAA J 2007;45(10):2448–57.
[57] Zhu Q, Shoele K. Propulsion performance of a skeleton-strengthened fin. J Exp Biol 2008;211:2087–100.
[58] Zhu Q, Wolfgang MJ, Yue DKP, Triantafyllou MS. Three-dimensional flow structures and vorticity control in fish-like swimming. J Fluid Mech 2002;468:1–28.